

1  
2  
3  
4  
5  
6  
7  
8  
9

---

This manuscript has been submitted for publication in Proceeding of the National Academy of Sciences, USA. Please note that the manuscript has not undergone peer-review and is not accepted for publication at this time. Subsequent versions of this manuscript may have slightly different content. If accepted, the final version of this manuscript will be available via the 'Peer-reviewed Publication DOI link on the right-hand side of this webpage. Please feel free to contact any of the authors; we welcome your feedback on our contribution to the literature.

---

10 Dynamics of Aggregates and Sinking Carbon Fluxes in a  
11 Turbulent Ocean

12 Draft: April 22, 2024

13 Authors: D.A. Siegel<sup>1,\*</sup>, A.B. Burd<sup>2</sup>, M. Estapa<sup>3</sup>, E. Fields<sup>1</sup>, L. Johnson<sup>4</sup>, E. Romanelli<sup>1,5</sup>,  
14 M.A. Brzezinski<sup>6</sup>, K.O. Buesseler<sup>7</sup>, S. Clevenger<sup>8</sup>, I. Cetinić<sup>9</sup>, L. Drago<sup>10</sup>, C.A. Durkin<sup>11</sup>,  
15 R. Kiko<sup>12</sup>, S.J. Kramer<sup>11</sup>, A. Maas<sup>13</sup>, M. Omand<sup>14</sup>, U. Passow<sup>15</sup>, and D.K. Steinberg<sup>16</sup>

16 1 - Earth Research Institute and Department of Geography, University of California, Santa  
17 Barbara, Santa Barbara, CA, USA, [david.siegel@ucsb.edu](mailto:david.siegel@ucsb.edu) & [fields@ucsb.edu](mailto:fields@ucsb.edu)

18 2 – Department of Marine Sciences, University of Georgia, Athens, GA, USA, [adrianb@uga.edu](mailto:adrianb@uga.edu)

19 3 – School of Marine Sciences, Darling Marine Center, University of Maine, Walpole, ME, USA,  
20 [margaret.estapa@maine.edu](mailto:margaret.estapa@maine.edu)

21 4 - Applied Physics Laboratory, University of Washington, Seattle, WA, [leahjohn@uw.edu](mailto:leahjohn@uw.edu)

22 5 - Institute of Environmental Engineering, Department of Civil, Environmental and Geomatic  
23 Engineering, ETH Zurich, Zurich, Switzerland, [eromanelli@ethz.ch](mailto:eromanelli@ethz.ch)

24 6 - Marine Science Institute, University of California, Santa Barbara, Santa Barbara, CA, USA,  
25 [mark.brzezinski@lifesci.ucsb.edu](mailto:mark.brzezinski@lifesci.ucsb.edu)

26 7 - Department of Marine Chemistry & Geochemistry, Woods Hole Oceanographic Institution,  
27 Woods Hole, MA 02543, USA, [kbuesseler@whoi.edu](mailto:kbuesseler@whoi.edu)

28 8 - MIT-WHOI Joint Program in Oceanography, Applied Ocean Science and Engineering,  
29 Cambridge, MA, United States, [samclev@mit.edu](mailto:samclev@mit.edu)

30 9 - GESTAR II, Morgan State University, Baltimore, MD, USA and Ocean Ecology Laboratory,  
31 NASA Goddard Space Flight Center, Greenbelt, MD, USA, [ivona.cetinic@nasa.gov](mailto:ivona.cetinic@nasa.gov)

32 10 - Laboratoire d'Océanographie de Villefranche, Sorbonne Université, Paris, France and  
33 Sorbonne Université, UMR 7159 CNRS-IRD-MNH, LOCEAN-IPSL, Paris, France  
34 [laetitia.drago@imev-mer.fr](mailto:laetitia.drago@imev-mer.fr)

35 11 - Monterey Bay Aquarium Research Institute, Moss Landing, CA, USA, [cdurkin@mbari.org](mailto:cdurkin@mbari.org) &  
36 [skramer@mbari.org](mailto:skramer@mbari.org),

37 12 - Laboratoire d'Océanographie de Villefranche, Sorbonne Université, Paris, France &  
38 GEOMAR Helmholtz Centre for Ocean Research Kiel, Germany, [rkiko@geomar.de](mailto:rkiko@geomar.de)

39 13 - Bermuda Institute of Ocean Sciences, School of Ocean Futures, Arizona State University,  
40 St. George's, Bermuda, [amaas4@asu.edu](mailto:amaas4@asu.edu)

41 14 - Graduate School of Oceanography, University of Rhode Island, Narragansett, RI, USA,  
42 [momand@uri.edu](mailto:momand@uri.edu)

43 15 - Ocean Sciences Centre, Memorial University Newfoundland, St. John's, NL, Canada &  
44 Marine Science Institute, University of California, Santa Barbara, Santa Barbara, CA, USA,  
45 [uta.passow@mun.ca](mailto:uta.passow@mun.ca)

46 16 – Coastal and Ocean Processes Section, Virginia Institute of Marine Science, William &  
47 Mary, Gloucester Point, VA, USA, [debbies@vims.edu](mailto:debbies@vims.edu)

48

49 \* - corresponding author

50 Abstract:

51 The sinking of particulate matter from the upper ocean dominates the export and  
52 sequestration of organic carbon by the biological pump, a critical component of the  
53 Earth's carbon cycle. Controls on carbon export are thought to be driven by ecological  
54 processes that produce and repackage sinking biogenic particles. Here, we present  
55 observations during the demise of the Northeast Atlantic Ocean spring bloom illustrating  
56 the importance of storm-induced turbulence on the dynamics of sinking particles. A  
57 sequence of four large storms caused upper layer mean turbulence levels to vary by  
58 more than three orders of magnitude. Large particle (>0.1 to 10 mm) abundance and  
59 size changed accordingly: increasing via shear coagulation when turbulence was  
60 moderate and decreasing rapidly when turbulence was intense due to shear  
61 disaggregation. Particle export was also tied to storm forcing as large particles were  
62 mixed to depth during mixed layer deepening. After the mixed layer shoaled, these  
63 particles, now isolated from intense surface mixing, grew larger and subsequently sank.  
64 This sequence of events matched the timing of sinking particle flux observations.  
65 Particle export was influenced by increases in aggregate abundance and porosity,  
66 which appeared to be enhanced by the repeated creation and destruction of  
67 aggregates. Last, particle transit efficiency through the mesopelagic zone was reduced  
68 by presumably biotic processes that created small particles (<0.5 mm) from larger ones.  
69 Our results demonstrate that ocean turbulence significantly impacts the nature and  
70 dynamics of sinking particles, strongly influencing particle export and the efficiency of  
71 the biological pump.

72 Significance Statement:

73 The ocean's biological pump, a critical component of the Earth's carbon cycle,  
74 transports organic matter from the surface ocean to depth. It is dominated by the  
75 sinking of organic particles, often in the form of large (>1 mm) marine snow aggregates.  
76 Here, we present observations during the demise of the North Atlantic spring bloom  
77 illustrating the important roles that storm-generated turbulence has on the abundance  
78 and characteristics of sinking aggregates. Turbulence creates and destroys aggregates  
79 and the vertical mixing induced enhances the transport of particles to depth. Evidence  
80 of biological processes, such as the creation of small particles from large ones likely  
81 due to zooplankton, is also observed. In all, these observations illustrate the complex  
82 interplay of physical and biological processes regulating the ocean's biological pump  
83 and the challenges in creating a predictive understanding of its functioning.

84 Keywords

85 Biological Carbon Pump, Marine Snow, Aggregate Dynamics, Ocean Turbulence, Sinking  
86 Particle Fluxes

## 87 Introduction

88 The ocean's biological pump transports organic matter, created by phytoplankton  
89 productivity in the well-lit surface ocean, to the ocean's dark interior, where it is  
90 consumed by animals and heterotrophic microbes and remineralized back to inorganic  
91 forms (Ducklow et al. 2001; LeMoigne, 2019; Iversen, 2023). This downward transport  
92 of organic matter, dominated by the gravitational settling of particles, sequesters  
93 respired carbon dioxide from exchange with the atmosphere on timescales of months to  
94 millennia, depending on the depth at which remineralization occurs and on ocean  
95 circulation and mixing processes (Siegel et al. 2023a; Nowicki et al. 2024). A predictive  
96 understanding of the biological pump function is critical to assess its role on future  
97 climate states and to measure the efficacy of carbon dioxide removal interventions  
98 aimed at contributing to net negative greenhouse gas emissions (Henson et al. 2022;  
99 NASEM, 2022).

100 Much of what has been learned about the ocean's biological pump has come from field  
101 studies where the life cycle of particles is followed from their production in the upper  
102 ocean to their export to depth (Ducklow et al. 2001; Siegel et al. 2016; Buesseler et al.  
103 2020). The sinking speed of most particles (roughly 50 to 100 m d<sup>-1</sup>) dictates a 5-to-10-  
104 day time scale to study the upper 500 m of the water column (estimated as the depth  
105 region of interest divided by a typical sinking time scale). Metrics for the efficiency of the  
106 biological pump, such as the e-ratio (export flux leaving the upper ocean divided by the  
107 net primary production, NPP), integrate biogeochemical fluxes over this time scale. The  
108 challenge arises when the biotic and abiotic factors vary on shorter time scales, such as  
109 during bloom events (Giering et al. 2017).

110 The rapid increase and subsequent decrease in phytoplankton biomass caused by the  
111 spring bloom in the subarctic oceans have long been of interest to oceanographers  
112 (Sverdrup, 1953; Ducklow and Harris, 1993, Siegel et al. 2002; Behrenfeld, 2010;  
113 Mahadevan et al. 2012). The North Atlantic spring bloom is characterized by the  
114 dominance of siliceous diatoms followed by a transition to mixed flagellate communities  
115 as the diatom dominated biomass sinks out of the upper ocean (Sieracki et al. 1993;  
116 Cetinić et al. 2015; Brzezinski et al, in review). The relationship between primary  
117 productivity and sinking particle export is thought to be a balance between bottom-up  
118 and top-down control (particle production vs. grazing) driven by the annual cycle of  
119 upper layer mixing (Wassmann, 1998; Laurenceau-Cornec et al. 2023). Here, we  
120 examine the demise of the North Atlantic spring bloom from the 2021 Export Processes  
121 in the Ocean from RemoTe Sensing (EXPORTS-NA) field campaign and demonstrate  
122 that abiotic physical processes, occurring on synoptic time scales, can be the dominant  
123 factor regulating the gravitational component of the biological carbon pump.

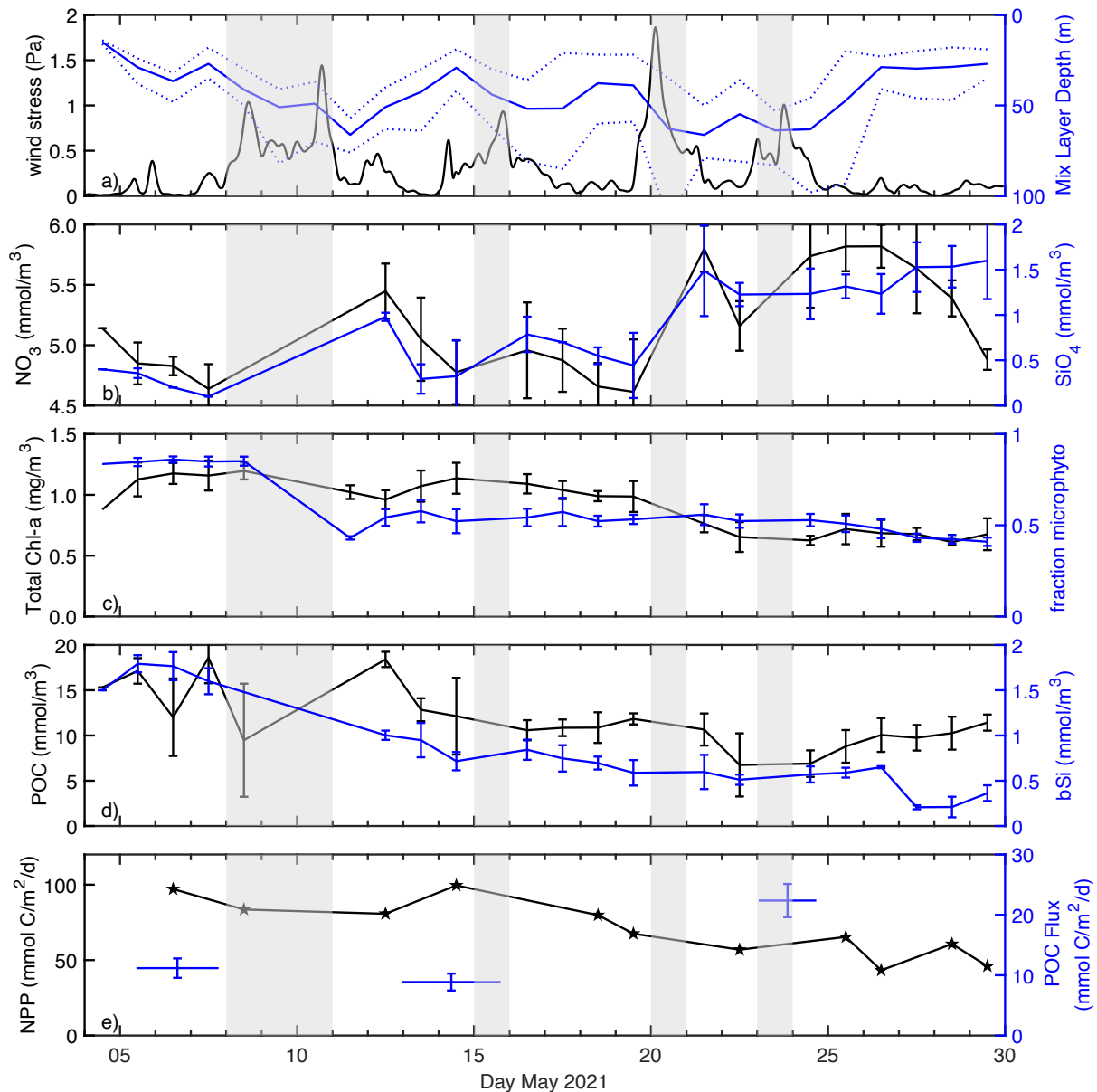
## 124 The oceanographic setting

125 The EXPORTS-NA field campaign was conducted within an anticyclonic eddy in the  
126 northeast Atlantic Ocean (see *Methods* and Johnson et al. 2024 for an assessment of  
127 the oceanographic conditions). An anticyclone was chosen as it would in principle retain  
128 water parcels within its core for the planned 25 days of sampling (Erickson et al. 2023).  
129 Multiple sampling assets were deployed with the goals of understanding temporal  
130 changes within the eddy's core and assessing the spatial/temporal changes outside of  
131 it. The location of the eddy center was monitored using multiple methods and the  
132 success of this approach was verified using an instrumented, Lagrangian float that  
133 remained near the eddy center at depth of roughly 75 m throughout the cruise (Erickson  
134 et al. 2023; Johnson et al. 2024). Water property analyses showed that in the eddy core  
135 waters (ECWs; below ~120 m), water parcels were retained throughout the experiment.  
136 Eddy core waters extended 15 km of the analyzed eddy center and measurements  
137 within this distance, regardless of depth, were deemed to be within the eddy (Johnson  
138 et al. 2024). However, in the surface core waters (SCWs) above the eddy core, a  
139 sequence of four intense storms (each with maximum hourly wind speeds exceeding 40  
140 kts) interrupted the ship-based sampling, deepened the mixed layer, and exchanged  
141 significant fractions of the SCWs with waters outside of the eddy due to Ekman  
142 transport (Figs. 1a & S1; Johnson et al. 2024).

143 Initially, the SCWs were characterized by extremely low silicate ( $\text{SiO}_4$ ) ( $<0.4 \mu\text{M}$ ),  
144 elevated nitrate ( $\text{NO}_3$ ) ( $\sim 5 \mu\text{M}$ ; Fig. 1b), moderate chlorophyll *a* concentrations ( $\sim 1.1 \text{ mg m}^{-3}$ ),  
145 and a dominance of microphytoplankton pigment biomarkers ( $\sim 80\%$  of the  
146 summed accessory pigment biomarkers; Fig. 1c). Together, this suggests that a bloom  
147 of diatoms had occurred previously and terminated due to  $\text{SiO}_4$  limitation (Sieracki et al  
148 1993; Cetinić et al. 2015; Brzezinski et al. in review). Analysis of the upper ocean silica  
149 and nitrogen budgets indicates that  $\sim 70\%$  of the diatom bloom had already been  
150 exported from the mixed layer before our arrival (Brzezinski et al. in review). The  
151 remaining nitrate supported the production of non-silicified phytoplankton during our  
152 field occupation and storm-induced, mixed layer entrainment supported intermittent  
153 diatom production (Fig. S2; Meyer et al. 2023; Brzezinski et al. in review). This dual-  
154 phase bloom scenario is typical of the North Atlantic spring bloom (Sieracki et al. 1993).  
155 Thus, we here focus on the second phase of the North Atlantic spring bloom and its  
156 associated particle export.

157 Most surface layer biogeochemical variables were highest upon arrival at the eddy and  
158 decreased over time, including: chlorophyll *a*, particulate organic carbon (POC) and  
159 biogenic silica concentrations, the contribution of microphytoplankton pigments to  
160 accessory pigments, and water column integrated rates of net primary production (NPP)  
161 (Fig. 1cde; Johnson et al. 2024; Brzezinski et al. in review; Meyer et al. 2023). Notably,  
162 vertically integrated rates of NPP decreased by  $>50\%$ . The first storm event (May 7-11)

163 had a large impact on the retention of SCWs and ~75% of these were exchanged with  
 164 waters from outside of the eddy core region, while daily mean mixed-layer depths  
 165 deepened from 22 to 68 m (Johnson et al. 2024).



166  
 167 **Figure 1: Time series of oceanographic conditions in surface core waters during the**  
 168 **EXPORTS-NA study.** Shown are time series of a) wind stress (black; left) and daily minimum,  
 169 mean and maximum mixed layer depth (blue; right), b) mixed layer mean nitrate ( $\text{NO}_3$ ; black;  
 170 left) and silicate ( $\text{SiO}_4$ ; blue right) concentrations, c) mixed layer daily mean total chlorophyll a  
 171 concentrations (black; left) and fraction of microphytoplankton pigments of the summed  
 172 accessory pigment biomarkers (blue; right; following Uitz et al. 2006), d) mixed layer mean  
 173 particulate organic carbon (POC; black; left) and biogenic silica (bSi; blue; right) concentrations  
 174 and e) water column integrated rates of net primary production (NPP; black) and POC export  
 175 fluxes measured at roughly 100 m using sediment traps (blue; right; see Table S1 for details).  
 176 All measurements shown were made within 15 km of the eddy center.

177 While NPP decreased two-fold in the field study, upper ocean sinking POC fluxes  
178 increased two-fold from the first to the third sediment trap deployments (Fig. 1e; Table  
179 S1). Comparing the POC flux at ~100 m to the POC stocks above it provides a measure  
180 of turnover of POC due to export from the upper ocean. These export turnover times  
181 were 2 to 3 months during the first two sediment trap deployments and about one month  
182 for the last. Turnover times for the production of POC ( $= \text{POC inventory} / \text{NPP}$ ) were  
183 considerably shorter (1 to 2 weeks; Table S1), illustrating that much of the fixed organic  
184 carbon was utilized by the upper ocean ecosystem and not exported to depth. However,  
185 both lines of evidence suggest a residence time of upper ocean POC stocks of >1 week.

## 186 Large particle distributions

187 Abundance-size distributions of large particles (~0.1 to 10 mm) were quantified as a  
188 function of depth using imagery collected by three Underwater Vision Profilers (UVPs;  
189 Picheral et al. 2010; see *Methods*). Focus here is on selected daily mean profiles of  
190 particle volume spectra presented in differential form (Fig. 2a; units are ppmV per mm  
191 bin width). Initially, high volumes of particles smaller than 1 mm were present in the  
192 mixed layer while comparatively low particle volumes of any size were found in the  
193 ECWs (Fig. 2a). From May 12-16, the maximum sizes of particles in the SCWs  
194 increased to greater than 3 mm, which may have been caused, at least in part, by  
195 horizontal exchanges of surface waters due to the storm-induced Ekman transport  
196 (Johnson et al. 2024). After May 15, a plume of large particles (>3 mm) appeared  
197 beneath the ML and over the next several days sank into the ECW. By May 25, the  
198 plume of large particles reached 500 m, implying an average sinking speed of  $\sim 33 \text{ m d}^{-1}$   
199 (300 m over 9 d). Post-bloom ecosystems in the North Atlantic often lead to rapid export  
200 of sinking particles from the surface ocean, but the delay between the first appearance  
201 of these particles in and just beneath the SCWs and their export was unexpected.

202 During the first 10 days of the study, daily mean particle volumes within the ECWs  
203 (depths  $\geq 120 \text{ m}$ ) were relatively low and dominated by smaller particles (Fig. 2a).  
204 However, outside the eddy core at similar depths, significantly more and larger particles  
205 were observed (Fig. 2b). In particular, the particle volume spectra there were similar to  
206 those observed later in the study within the ECW (after May 22; Fig. 2a). This suggests  
207 that the midwater depths outside of the eddy core had already been modified by the  
208 passage of sinking particle plumes, while this signal was absent within the ECWs until  
209 after May 15. Midwaters outside of ECW were likely enhanced by lateral mixing from a  
210 patchwork of export flux events given the high degree of spatial heterogeneity in the  
211 surface biological fields (example daily mean satellite chlorophyll distributions are  
212 shown in Fig. S1). The low abundance of large particles within the ECW observed  
213 initially confirms the high degree of water parcel retention in the anticyclone's ECW (due  
214 to potential vorticity conservation; Johnson et al. 2024). Importantly, the initial low

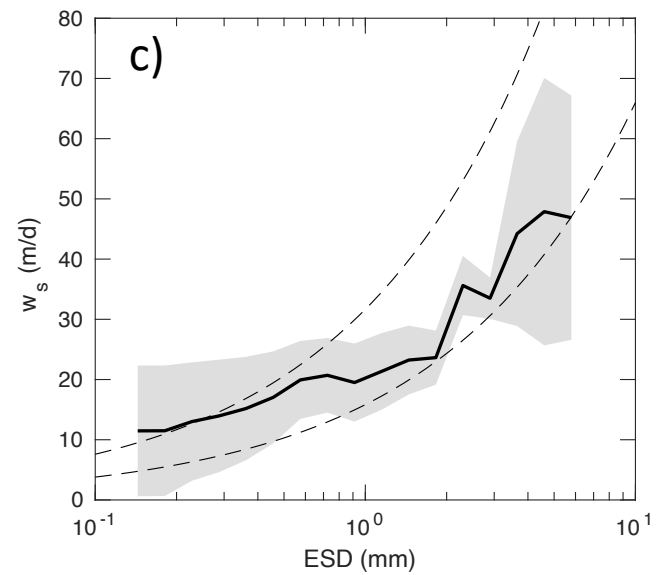
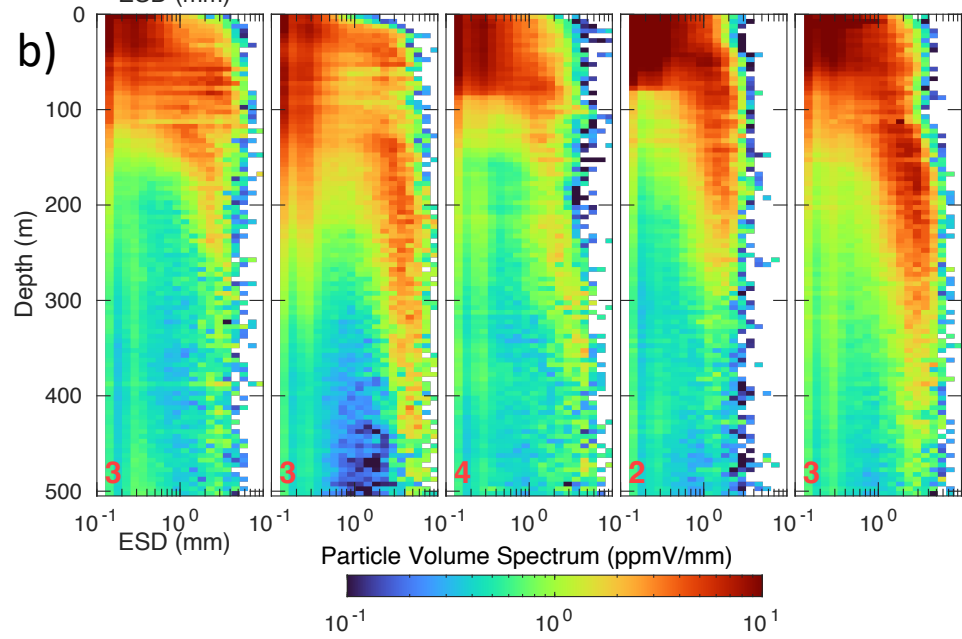
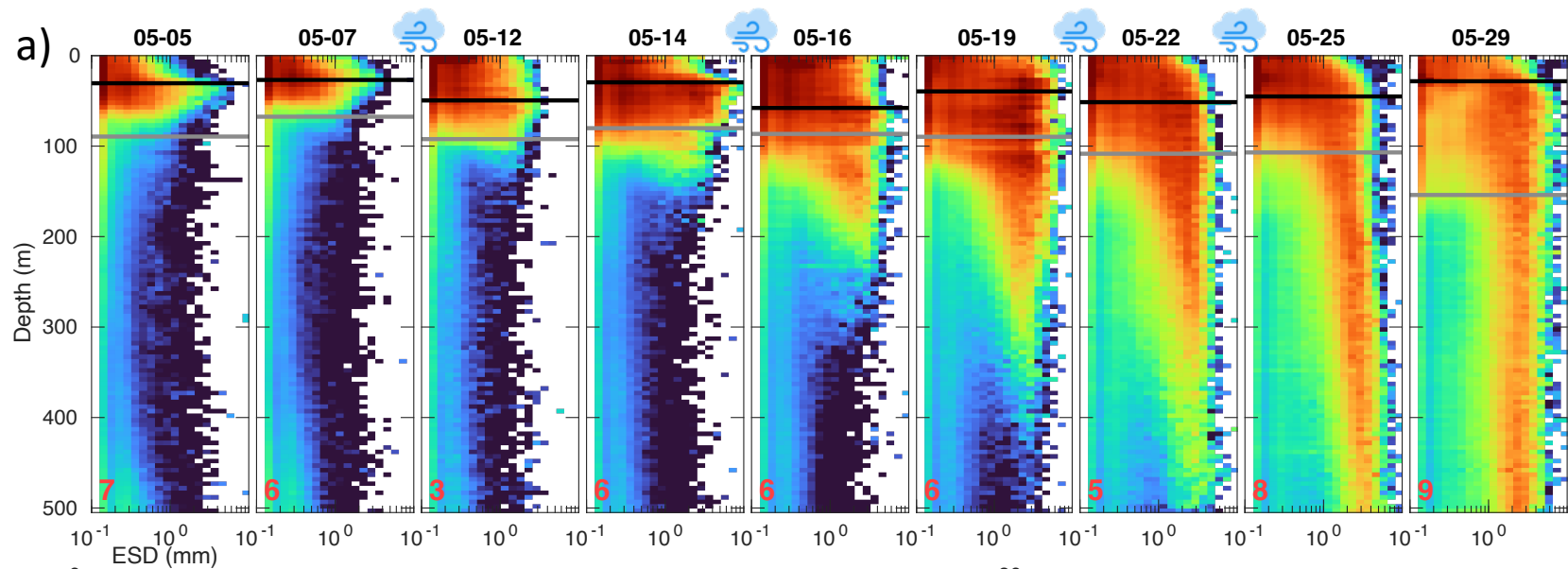
215 particle volumes in the ECW provide a nearly pristine environment for diagnosing the  
216 dynamical relationships among particles and sinking particle flux.

217 The sinking speed estimate suggested from large particle plume can be refined to  
218 assess sinking speed as a function of particle size. Here, the sinking speed size  
219 distribution,  $w_s(D)$ , was determined by assessing temporal changes in the depth of  
220 particle abundance isosurfaces for each size bin (see *Methods*). Values of  $w_s(D)$   
221 increased with size and ranged from  $\sim 10 \text{ m d}^{-1}$  to nearly  $50 \text{ m d}^{-1}$  for the largest  
222 particles assessed (Fig. 2c). These values correspond well with time mean estimates for  
223 fast-sinking particles determined from coordinated marine snow catcher (MSC) and  
224 sediment trap sampling (Romanelli et al. 2024) as well as theoretically derived sinking  
225 speed distributions (Kriest, 2002).

226

227 **Figure 2: Vertical profiles of the particle volume size distribution for selected days.** a)  
228 Daily mean, differential particle volume spectra (ppmV/mm) profiles for selected days during the  
229 cruise and within 15 km of the eddy center. Particle volume spectra are presented in differential  
230 form as they accentuate changes in the particle size spectra that are difficult to visualize using  
231 particle abundance spectra. Bins are logarithmically distributed with bin centers from 0.13 to  
232 10.3 mm. The black line denotes the daily mean MLD near the eddy center, while the gray line  
233 denotes the depth of the daily mean  $27.2 \text{ kg m}^{-3}$  isopycnal, which defines the upper boundary of  
234 the ECW (Johnson et al. 2024). The storm icons denote the four storm periods with intense  
235 winds and waves and interruption of the ship-based sampling. The number in the lower left  
236 corner of each spectrum profile is the number of UVP casts used to create the daily mean  
237 spectra. b) Daily mean particle volume spectra (ppmV/mm) profiles for selected days outside  
238 the eddy (15 to 60 km from eddy center). c) Mean particle sinking speed size distribution from  
239 following UVP particle abundance isosurfaces (black solid line); the standard deviation of the  
240 sinking speed estimates (gray shading); and two widely applied  $w_s(D)$  estimates (dashed lines)  
241 from Kriest (2002) (entries 8 & 9 in Table 2 in their paper).

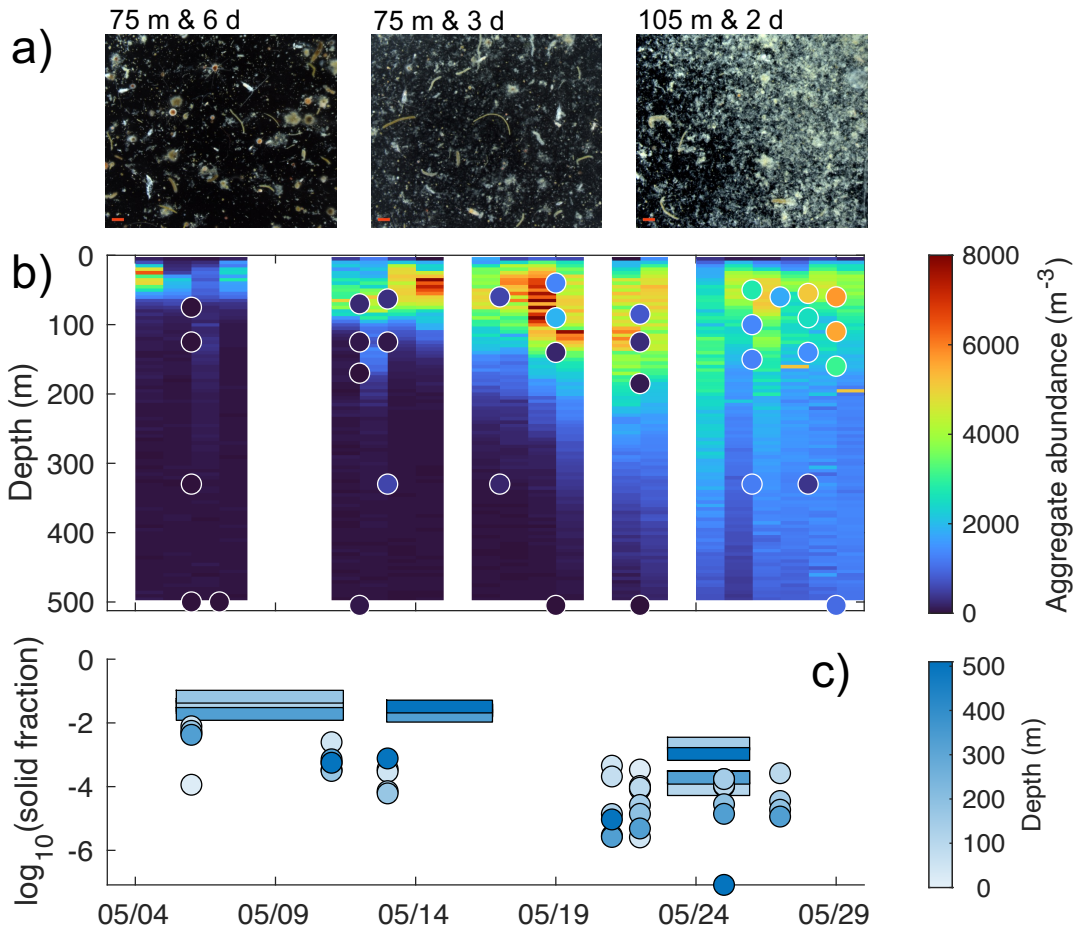




243 Structural changes of large particles throughout the water column

244 Knowledge of the physical structure of a particle is important for assessing its  
245 interactions with the environment and the organisms therein (Burd and Jackson, 2009;  
246 Laurenceau-Cornec et al. 2015; Iversen, 2023). Micrographs of sediment trap contents  
247 (Fig. 3a) show that large particles became more numerous, increased in size, became  
248 fluffier. Further, the trap collection periods decreased in the three trap deployments,  
249 indicating that the flux of large particles increased dramatically over the course of the  
250 study. These findings were corroborated by MSC observations of increased aggregate  
251 abundances after May 12 and a higher number of large (>0.1 mm), fast-sinking  
252 aggregates over time and with depth (Fig. 3b; Romanelli et al. 2024). Daily mean  
253 aggregate abundances, determined via automated classification of individual UVP  
254 thumbnail images (*Methods*), are consistent with the MSC results (Fig. 3b). Abundances  
255 of UVP-imaged aggregates show a similar increase after May 13 (Fig. 3c) and peak  
256 concentrations after May 24. Overall, more than 90% of the large particles (>1 mm)  
257 characterized from the individual UVP images were identified as aggregates. The  
258 correspondence between the three methods is reassuring, considering they quantify  
259 aggregates differently, either imaged from the bottom of a sediment trap, collected in a  
260 tray at the bottom of a marine snow catcher, or imaged *in situ*.

261 Large particles were extremely porous throughout the time series with solid particle  
262 fractions (defined as  $1 - \text{porosity}$ ) ranging from  $10^{-2}$  to  $10^{-6}$  (Fig. 3c). This range of solid  
263 particle fractions is similar to previous *in situ* field determinations (Alldredge and  
264 Gotschalk, 1988). However, during our study, the entire previously reported range was  
265 observed. Values of solid particle fraction decrease in time, but no obvious changes in  
266 its depth distribution were observed (Fig. 3c). Particle solid fractions were calculated as  
267 the ratio of solid particle component volumes estimated from the sample's composition,  
268 to the UVP-imaged total particle volumes (see *Methods*). Particle solid fraction was  
269 estimated by two different methods: from traps that collect sinking particles, and from  
270 large volume pump-UVP pairings that sample particles from the water column.  
271 Determinations of the solid particle fraction were higher for the sinking particles  
272 captured in traps than for particles imaged in the water column as expected; but both  
273 estimates decreased in time, indicating that the population of particles examined were  
274 becoming more porous (Fig. 3c). Together, these results demonstrate that the fractal  
275 nature of imaged particles must be considered in any quantitative analysis of particle  
276 mass using these tools (Logan and Wilkinson, 1990; Stemmann et al. 2004; Burd and  
277 Jackson, 2009).



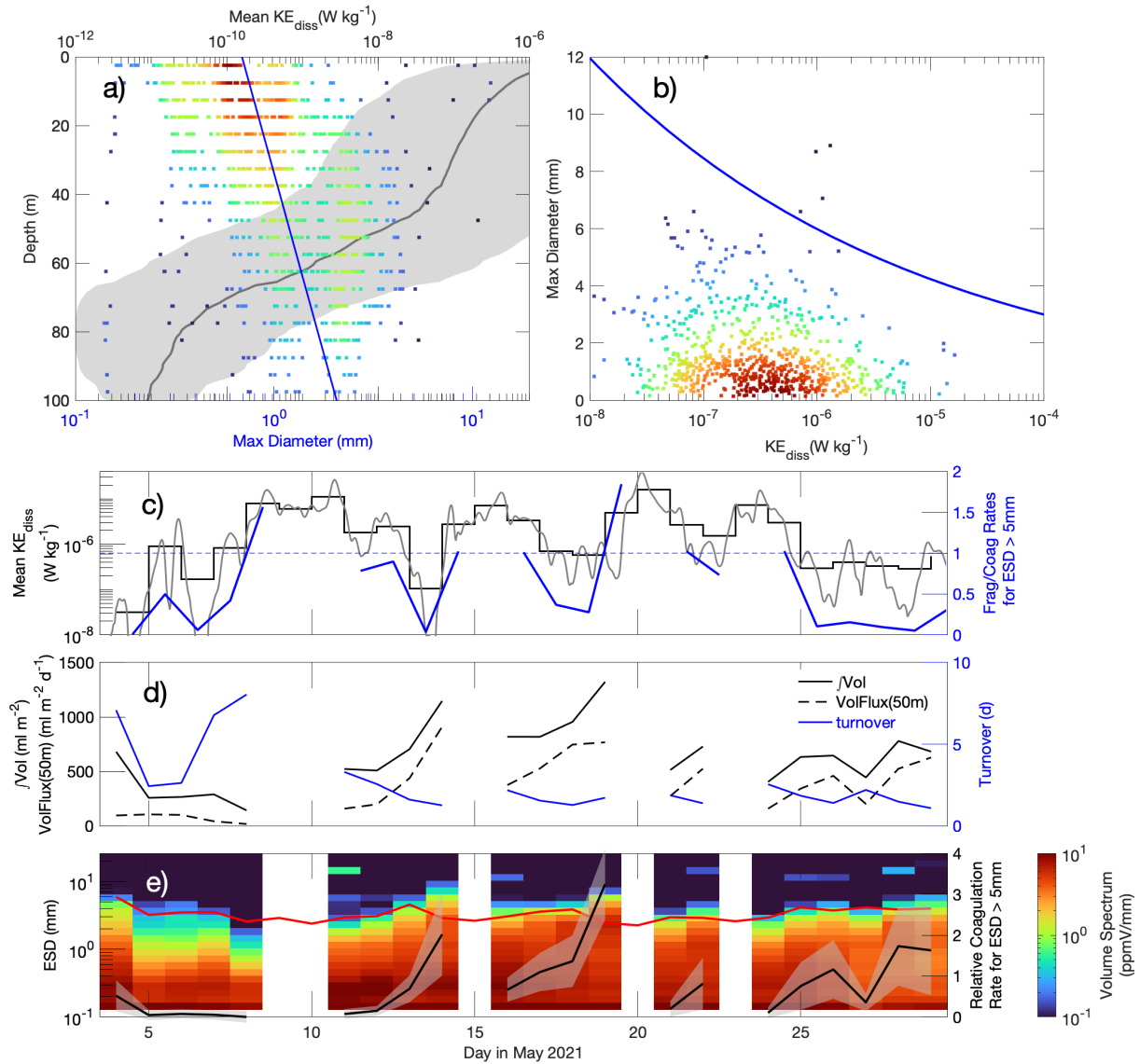
278

279 **Figure 3: Structural changes in large particle characteristics in time and depth.** a)  
 280 Representative micrographs of gel trap contents from the three sediment trap deployments for  
 281 size range of 50  $\mu\text{m}$  to 5 mm. Scale bars in lower left corners of images (red) are 1 mm.  
 282 Sampling depths and durations were 75 m and 6 days, 75 m and 3 days, and 105 m and 2 days  
 283 for the three collection periods. b) Aggregate abundance and composition estimates as function  
 284 of depth and time within the eddy center. UVP imaged aggregate abundance analysis are the  
 285 contours, while fast sinking, large aggregates hand collected from the MSC collections are the  
 286 filled circles. c) Solid particle fractions from geochemical/gel trap pairings (rectangles for which  
 287 length denotes the trap collection duration) and high-volume pump and UVP matchups (circles).  
 288 Depth of sample collections is shown in the color scale.

### 289 Abiotic controls on large particle dynamics in the surface layer

290 Our observations reveal several examples where abiotic, physical processes have  
 291 proximate controls on the dynamics of large particles. For example, large reductions in  
 292 particle volume and particle sizes occurred within the mixed layer close to the sea  
 293 surface where turbulence levels are highest (Figs. 2a & S4). This is particularly evident  
 294 on May 14, 22, and 25, when wind stress and thereby near surface turbulence levels  
 295 were elevated (Fig. 1a). Turbulent shear rates are important for particle dynamics, as a  
 296 moderate amount facilitates collisions among particles and promotes increases in

297 particle sizes via shear coagulation, while high turbulence levels disaggregate particles  
298 (Alldredge et al. 1990; Jackson, 1990; Burd & Jackson, 2009; Takeuchi et al. 2019).  
299 Relating the largest particle size ( $D_{\max}$ ) reliably sampled by the UVP (*Methods*) to  
300 turbulence levels within the mixed layer clearly shows the influence of mixed-layer  
301 turbulence on particle sizes. Over the entire study, maximum particle sizes within the  
302 mixed layer increased more than three-fold with depth, while turbulent kinetic energy  
303 dissipation rate,  $KE_{\text{diss}}$ , estimated from air-sea momentum and buoyancy fluxes  
304 (*Methods*), decreased rapidly (Fig. 4a). Maximum particle sizes near the surface are  
305 regulated, at least in part, by shear disaggregation due to elevated turbulence levels  
306 (Alldredge et al. 1990; Takeuchi et al. 2019) as evidenced by the decrease in maximum  
307 particle sizes with  $KE_{\text{diss}}$  when  $KE_{\text{diss}} > 10^{-7} \text{ W kg}^{-1}$ . Maximum particle sizes observed  
308 were only rarely reached the maximum aggregate size found in the laboratory  
309 experiments of Alldredge et al. (1990) (blue line in Fig. 4b). Classic turbulence scaling  
310 predicts mixed-layer turnover times of an hour or less (scaling as  $Z_{\text{ML}} / u^*$ , where  $Z_{\text{ML}}$  is  
311 the mixed-layer depth,  $u^*$  is the surface friction velocity =  $(\tau/\rho)^{1/2}$ ;  $\tau$  is wind stress and  $\rho$   
312 is seawater density); therefore, shear fragmentation must occur very quickly. Whereas  
313 turbulence levels near the surface favor smaller maximum particle size and  
314 fragmentation, those near the base of the mixed layer favor coagulation and larger  
315 particles. The largest particles were found at depth for intermediate values of  $KE_{\text{diss}}$  (Fig.  
316 4b), suggesting that there is a turbulence level, roughly  $5 \times 10^{-8} \text{ W kg}^{-1}$ , large enough to  
317 promote particle-particle encounters leading to coagulation, but not so large as to lead  
318 to disaggregation of those particles.



319

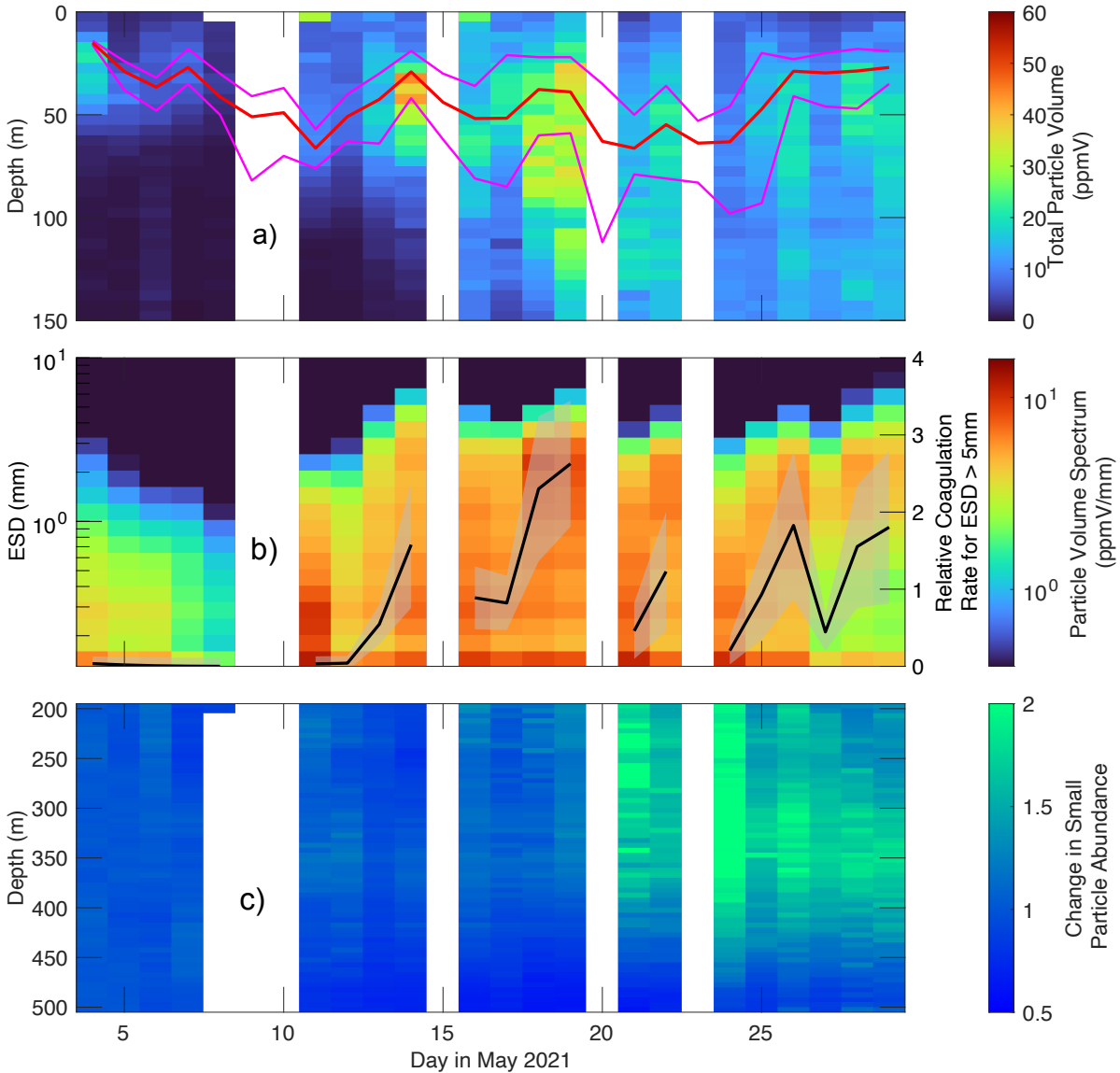
320 **Figure 4: Turbulence and large particle dynamics in the upper 50 m.** a) Individual  
 321 observations of the maximum particle size,  $D_{\max}$ , sampled by the UVP vs. depth within the  
 322 mixed layer (see *Methods* for how  $D_{\max}$  is estimated). Individual UVP observations and hourly  
 323  $KE_{\text{diss}}$  estimates are shown where the color represents the data density in  $D_{\max}$ -depth space (red  
 324 highest, blue lowest). The solid blue line is the best fit line of  $D_{\max}$  with depth. The black line and  
 325 gray envelope are the study mean and standard deviation envelope for the  $KE_{\text{diss}}$  vertical profile  
 326 within the mixed layer. b) Comparison of individual  $D_{\max}$  observations with  $KE_{\text{diss}}$  estimates. Data  
 327 are the same as in a). The color for each observation represents the data density in  $KE_{\text{diss}}$ -depth  
 328 space (again, red is highest). Blue solid line is the average maximum aggregate size found in  
 329 the laboratory study of Alldredge et al. (1990) ( $D_{\max} = 0.75 (KE_{\text{diss}})^{-0.15}$ ). c) Time evolution of the  
 330 mean  $KE_{\text{diss}}$  in the upper 50 m (black; hourly & daily) and the ratio of modeled particle  
 331 fragmentation to particle growth via coagulation for particles larger than 5 mm (blue line; >1  
 332 fragmentation dominates, < 1 coagulation). d) Total particle volume inventory, particle volume  
 333 sinking flux at 50 m and their turnover time. e) Upper 50 m mean particle volume spectra as  
 334 function of time. Black lines are modeled time series of relative coagulation rates for large

335 particles in the upper 50 m. The uncertainty envelope for coagulation rates illustrates the  
336 variations in the ensemble created using a range of fractal dimension scenarios. Also plotted  
337 (red line) is the maximum marine snow size as function of upper layer  $KE_{diss}$  based upon the  
338 laboratory experiments of Alldredge et al. (1990).

339 Over the observational period, daily mean estimates of  $KE_{diss}$  averaged over the upper  
340 50 m of the water column varied by more than three orders of magnitude due to the  
341 presence or absence of storms (Fig. 4c). As a result, particles larger than 5 mm had a  
342 high potential for fragmentation during storm events, while they were more apt to grow  
343 during the quiescent periods between storms due to shear coagulation (Fig. 4c; see  
344 *Methods* for calculation details). The effects of the storms are evident in the upper layer  
345 integrated total particle volumes measured when ship operations resumed after the  
346 storms passed (Fig. 4d). Particle volumes were low just after each storm passed and  
347 then increased rapidly. After the first two storms (May 11-14 & May 16-19), total particle  
348 volumes increased nearly two-fold in just a few days. Changes in the upper-layer mean  
349 particle volume size spectra mirrored changes in the turbulence levels where particle  
350 sizes and volumes grew when turbulence levels were low and decreased when  
351 turbulence was high (Fig. 4e). This is reflected in temporal patterns in formation rates of  
352 particles  $> 5$  mm by coagulation. Initially, upper-layer coagulation rates were small due  
353 to both low turbulence and a scarcity of particles large enough to coagulate efficiently  
354 (Fig. 4e). After each storm, particle coagulation rates for particles  $> 5$  mm in size  
355 increased dramatically as the lower turbulence levels promoted coagulation and the  
356 production of particles large enough to coagulate to yet larger ones. Thus, the dynamics  
357 of upper layer large particles ( $> 5$  mm) is driven by fragmentation when turbulence is  
358 high (upper layer mean  $KE_{diss}$  greater than about  $10^{-6} W kg^{-1}$ ) and coagulation when  
359 turbulence is low (Fig. 4c). Together, these data illustrate the highly ephemeral nature of  
360 large aggregates in the upper ocean as perturbed by intense storm conditions.

361 The storm events also influenced large particle dynamics by rapidly altering the depth of  
362 the surface mixed layer, which in turn impacted the vertical transport of large particles  
363 and turbulence levels (Fig. 1a). As noted above, a pulse of sinking particles was  
364 observed traversing from the base of the mixed layer starting on May 14 and reaching  
365 500 m on about May 25 (Fig. 2a). However, it is unclear what drove the timing of the  
366 sinking particle flux event. Initially (May 7), the UVP-imaged particle volume spectra  
367 showed very few particles  $> 1$  mm below the mixed layer (Fig. 2a). After the first storm  
368 (May 12 and 14), larger particles were observed both within the mixed layer, but also  
369 below this depth. The first storm not only exchanged SCWs with waters from outside the  
370 eddy, but it also deepened the mixed layer from 22 to 68 m (Fig. 5a; Johnson et al.  
371 2024). After the storm passed, the mixed layer shoaled rapidly, effectively exporting  
372 particles beneath the shallower mixed layer into the depth interval from 22 to 68 m, in a  
373 process similar to the seasonal mixed layer pump (Dall'Olmo et al. 2016). Evaluating  
374 this for all storm events, both particle sizes and total particle volume between the depth

375 interval from 40 to 80 m rapidly increased in between storms (Figs. 5a & b). Temporal  
 376 patterns in the relative coagulation rates of large particles ( $> 5 \text{ mm}$ ) for the 40 to 80 m  
 377 layer support the idea that coagulation was a significant driver of this increase (Fig. 5b).



378

379 **Figure 5: Dynamics of large particles at depth.** a) Total particle volume depth-time series  
 380 from the large ( $> 0.1\text{mm}$ ) particle imagery (ppmV). Shown also in the red and pink lines are the  
 381 daily minimum, mean, and maximum mixed layer depths from the instrumented glider which  
 382 profiled roughly every two hours near the eddy center (Johnson et al. 2024). b) Daily mean  
 383 particle volume spectrum averaged for the layer between 40 to 80 m as a function of particle  
 384 size. Overlaid are modeled time series of relative coagulation rates for large particles in the  
 385 same layer where the uncertainty envelope illustrates the variation in the ensemble created  
 386 using different fractal dimension scenarios. c) Relative changes in the vertical profile of the  
 387 abundances of small particles ( $0.13 > D > 0.51 \text{ mm}$ ) with depth and time relative to the mean  
 388 profile from May 4 and 5.

389 The coupled turbulent and particle dynamics provide an explanation for the timing of the  
390 pulse of sinking large particles. Initially, large ( $> 5$  mm) particle coagulation rates were  
391 extremely low in the 40 to 80 m layer. After the first storm, these rates increased rapidly  
392 as the abundance of particles available to make large aggregates increased, due to  
393 mixed layer pumping as well as via coagulation due to the moderate turbulence levels.  
394 These large particles then sank at velocities of order  $50 \text{ m d}^{-1}$  (Fig. 2c), sinking into the  
395 ECWs as can be seen on May 12 and 14 (Fig. 2a). The following storm, on May 15,  
396 accelerated this process. These analyses illustrate that the large observed particle  
397 export pulse resulted from a complex combination of processes, including mixed layer  
398 entrainment and detrainment transporting large particles to depth, shear coagulation,  
399 and finally the sinking of the large particles into the eddy interior.

400 Last, repeated storm forcing suggests there was a successive reworking of particles in  
401 the upper ocean leading to increased particle porosity in time. This may have led to the  
402 explosive growth of large aggregates ( $> 5$  mm) later in the study. Evidence for this can  
403 be found by evaluating the turnover time scales for POC and particle volumes in the  
404 upper 100 m of the water column. Turnover time scales for POC production  
405 ( $\dot{V}_{\text{POC}}/\text{NPP}$ ) were about a week or two, while turnover time estimates for POC export  
406 were months (Table S1). Contrasting this, turnover times for large particle volumes  
407 ( $\dot{V}_{\text{Vol}}/\text{VolFlux}(100\text{m})$ ) were about a week at the beginning of the cruise and decreased to  
408 about a day (Table S1). This implies that large particles were being rapidly built and  
409 exported, yet most of the particle mass, as measured by the POC concentration, was  
410 retained in the upper ocean. In fact, more than 90% of the POC in the MSC collections  
411 was found in the suspended fraction (Romanelli et al. 2024).

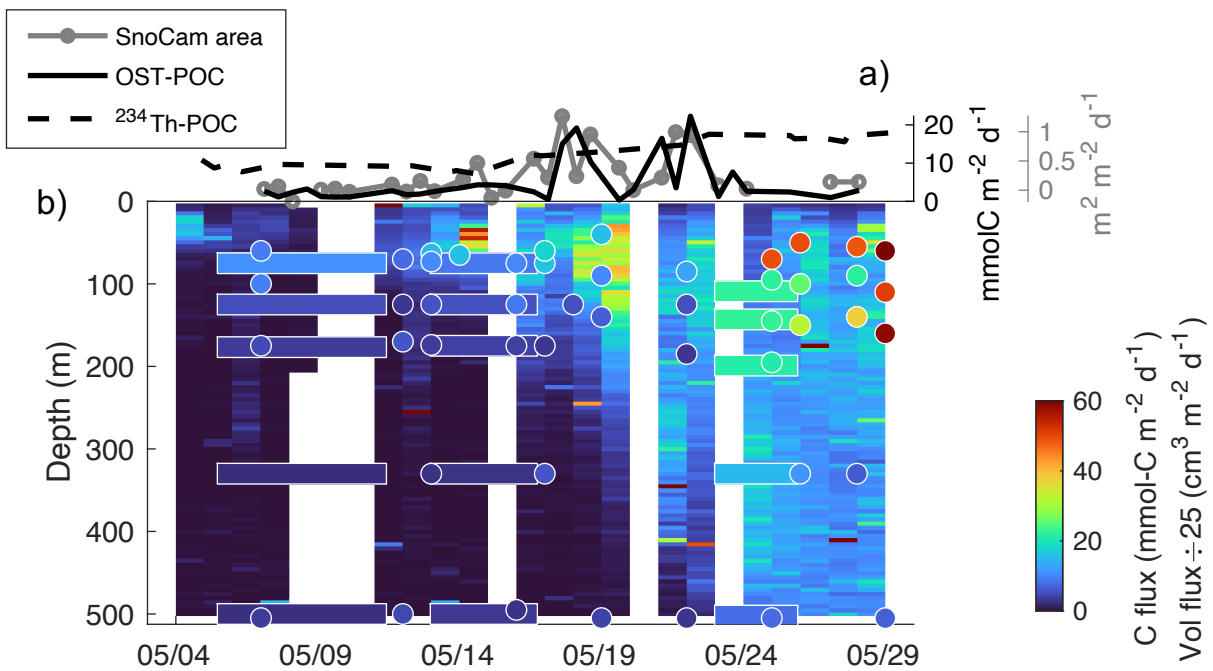
412 We suggest that the processes of sequential building and destroying of aggregates in  
413 the mixed layer may lead to a pool of particles whose porosity increases over time.  
414 Turbulence limits the size of aggregates by shearing them into two or more fragments  
415 by the smallest eddies in the flow, the Kolmogorov scale (Alldredge et al. 1990;  
416 Takeuchi et al. 2019). Laboratory experiments showed that individual shear  
417 disaggregation events result in pairs of fragment particles most of the time (Alldredge et  
418 al. 1990; Song et al. 2024). These fragments should have a similar fractal nature to their  
419 parent and when coagulated again, the resulting aggregates should become even more  
420 fractal and porous. This hypothesis is consistent with observations of particle porosity  
421 growing over time during the experiment (Fig. 3c).

## 422 Particle Dynamics and Sinking Particle Carbon Export

423 Changes in the particle size distribution illustrate a net transport of large particles to  
424 depth (Fig. 2a) and likely an export of organic carbon to depth. However, given the large  
425 degree of porosity and its changes over time (Fig. 3c), correspondence between imaged  
426 particles and sinking POC fluxes is not guaranteed. Here, we compare estimates of



427 sinking particle volume fluxes, determined from the imaged large particle distribution  
 428 and an assumed sinking particle velocity size distribution (see *Methods*), to more  
 429 traditional measurements of sinking particle export.



430  
 431 **Figure 6: Sinking POC fluxes and proxy measurements.** a) Sinking POC fluxes over time  
 432 from different flux proxies. The black line shows the POC flux from the Optical Sediment Trap  
 433 (OST); the brown line is the particle area flux sampled by the SnoCAM; and the black dashed  
 434 line is the POC flux estimated from deficits of  $^{234}\text{Th}$  at 75 m (Fig. 9 in Clevenger et al. 2024).  
 435 The mean ( $\pm$  sd) depth of the OST and SnoCAM measurements was  $75 \pm 14$  m. b) POC fluxes  
 436 from geochemical sediment traps (rectangles), the marine snow catcher (circles) and UVP-  
 437 determined particle volume flux estimates (contours). All measurements were made near the  
 438 eddy center and are scaled to the common color bar.

439 Sinking particulate organic carbon (POC) fluxes were determined directly during  
 440 deployments of surface tethered and neutrally buoyant sediment traps, as well as by  
 441 several other flux sampling tools that provide proxy determinations and complimentary  
 442 information (Fig. 6). These include optical sediment traps, globally calibrated to provide  
 443 estimates of sinking POC fluxes (OST-POC; Estapa et al. 2023), a prototype, upward-  
 444 viewing time lapse camera mounted on the Lagrangian float (SnoCAM),  $^{234}\text{Th}$ -derived  
 445 POC fluxes (Clevenger et al. 2024), analysis of the fast-sinking components of POC in  
 446 the MSC collections (Romanelli et al. 2024), and determinations of the particle volume  
 447 sinking flux from in situ particle imaging (see *Methods*). Sinking particle fluxes and their  
 448 proxies all show similar patterns with increasing fluxes in time and this increasing signal  
 449 propagating to depth over time. Before May 16, POC fluxes were relatively low with  
 450 strong attenuation beneath the mixed layer (Fig. 6b). From May 14 to May 23, sediment  
 451 trap-measured POC fluxes increase by a factor of two in the upper ocean and that  
 452 increase in fluxes propagated to depth. This change in flux was also detected by the

453 <sup>234</sup>Th-derived POC fluxes (Fig. 6a). Sinking particle fluxes determined from the marine  
454 snow catcher collections follow this same pattern, but show a dramatic increase in flux  
455 after May 25 reaching ~60 mmol-C m<sup>-2</sup> d<sup>-1</sup> in the upper layers (Romanelli et al. 2024).  
456 This late increase is supported by <sup>234</sup>Th-derived POC fluxes at 95 m (Clevenger et al.  
457 2024). The optical sediment traps and SnoCAM detected a large increase in particle  
458 export at ~80 m, matching the initial patterns detected in the UVP particle volume  
459 fluxes. However, flux determinations from the optical sediment traps and SnoCAM  
460 decreased sharply after May 23, potentially due to spatial heterogeneity in sinking fluxes  
461 and/or an under sampling by the small-cross section beam transmissometer in the case  
462 of the OST (Estapa et al. 2023), and low sensitivity of the prototype SnoCAM to large,  
463 low fractal-dimension aggregates as were observed later in the study (Fig. 3bc).

464 Overall, particle dynamics and particle sinking determined from the time course of  
465 particle volume fluxes from UVP imagery correspond well with the POC export  
466 determined from the other approaches (Fig. 6b). The general increase in the sinking  
467 particle volume fluxes in both time and depth corresponds with the direct and proxy  
468 sinking POC fluxes. Correspondence was also good with the MSC-derived POC fluxes,  
469 although the MSC fluxes are considerably higher in the upper 200 m late in the  
470 observational record and suggest lower flux transmission values. Although this is not a  
471 quantitative comparison of POC flux measurement methods (a subject of future work), it  
472 does support the use of particle imagery of large particle distributions for understanding  
473 vertical flux processes in the upper ocean.

## 474 Biotic Controls on Particles in the Upper Mesopelagic Zone

475 Apparent biotic controls on the particle size distribution can also be quantified in the  
476 upper mesopelagic zone of the eddy core waters. After May 20, abundance of small  
477 (≤0.51 mm) particles within the ECW increased by a factor of more than two compared  
478 to May 4-5 (Fig. 5c). It is unlikely these smaller particles sank from the surface ocean  
479 given the time required for these presumably slow-sinking particles to traverse many  
480 100's of meters (Fig. 2c). Horizontal advection can also be ruled out due to the retentive  
481 nature of the eddy and KE<sub>diss</sub> levels are too low for significant shear disaggregation to  
482 occur. More likely, the observed increase in small particles is driven by biological  
483 processes, such as the destruction of large particles by zooplankton via sloppy feeding  
484 and/or animal-generated shear (Dilling and Alldredge, 2000; Steinberg and Landry,  
485 2017).

486 Support for this hypothesis can be found in estimates of the encounter rate between  
487 large (>0.51 mm) particles and zooplankton (see *Methods*). For the three days where  
488 simultaneous zooplankton and large particle data were available, estimated encounter  
489 rates increased by factors of 10 to nearly 30-fold from May 11 to May 26 (Table S2).  
490 This was due to a modest increase in zooplankton abundance (2x) and a strong

491 increase in large particle abundances (>10x), consistent with the suggestion that the  
492 disaggregation of large particles by zooplankton created these smaller particles.

493 The imaged particle data can be used to quantify the rate of small particle (< 0.51 mm)  
494 production from large ( $\geq 0.51$  mm) particles using a two size-class model of particle  
495 abundance (Jackson and Burd, 2015). The model (Eq. 1) relates the time rate of  
496 change of small and large particle abundance to the sum of their sinking through the  
497 water column, the transformation of large particles to small ones with a specific rate  $\beta$ ,  
498 and the consumptive losses of each with a specific rate  $\gamma$ , or

$$499 \quad \frac{\partial P_S}{\partial t} = w_S \frac{\partial P_S}{\partial z} + \beta P_L - \gamma P_S \quad (1a)$$

$$500 \quad \frac{\partial P_L}{\partial t} = w_L \frac{\partial P_L}{\partial z} - \beta P_L - \gamma P_L \quad (1b)$$

501 Abundance of large and small particles (and their gradients with respect to time and  
502 depth) was estimated via in situ particle imaging, with particle mass determined  
503 assuming an ensemble of particle fractal dimension values to account for particle  
504 porosity, and the model coefficients determined by linear regression (See *Methods*).

505 The mean rate of transformation of large to small particles ( $\beta$ ) is small (0.010 [0.006  
506 s.d.] d<sup>-1</sup>) yet positive for all ensemble members, demonstrating there is a net production  
507 of small particles from large ones. This estimated rate corresponds to nearly a 30%  
508 increase in small particle abundance for the 25-day experimental period, accounting for  
509 some, but not all of the observed, two-fold increase shown in Figure 5c. The net  
510 production of small particles from large ones occurs simultaneously with a large  
511 increase in zooplankton-to-large particle encounter rates suggesting that zooplankton-  
512 particle interactions, via zooplankton consumption, sloppy feeding, fragmentation by  
513 swimming action, or a combination thereof, is the likely source (Dilling et al. 1998;  
514 Dilling and Alldredge, 2000; Goldthwait et al. 2004; Steinberg and Landry, 2017).  
515 Sloppy feeding will also enhance the solubilization of particles into dissolved forms  
516 which are widely available to the mesopelagic microbial community (Møller et al. 2003;  
517 Collins et al. 2015).

518 The two size-class model results also support several of our previous findings. For  
519 example, modeled large and small particle sinking speeds were 68.9 (2.7 s.d.) m d<sup>-1</sup>  
520 and 12.1 (1.6 s.d.) m d<sup>-1</sup>, respectively, consistent with assessments presented here (Fig.  
521 1c) and study-mean determinations of sinking particle settling speeds made using  
522 paired MSC and sediment trap collections (Romanelli et al. 2024). The retrieved specific  
523 consumption rate ( $\gamma = 0.118$  [0.008 s.d.] d<sup>-1</sup>), is considerably higher than microbial O<sub>2</sub>  
524 consumption rates made on individual particles at this site (Belcher et al. 2016), but it  
525 suggests that the consumption and fragmentation by grazers contributes substantially to  
526 particle losses.

## 527 Implications

528 The observations presented here show that physical dynamics of the upper ocean can  
529 play a key role in particle transformations and the efficiency of sinking carbon export  
530 from the upper ocean. Mixed layer turbulence is required to produce and maintain a  
531 pool of large particles that sink to depth, yet too much turbulence fragments the largest  
532 particles, thereby decreasing their sinking velocities and export potential. The passage  
533 of storms deepened the mixed layer, which then rapidly shoaled as the storms passed,  
534 leading to the isolation of particles roughly 30 m beneath the mixed layer. There, these  
535 particles were protected from the intense turbulent shear levels and the lower  
536 turbulence levels enabled increases in particle size through coagulation and thereby  
537 higher sinking rates. Last, the repeated storm forcings and turnover time scales for  
538 upper ocean POC and total particle volumes suggest a reworking of particles in the  
539 upper ocean leading to increasing particle porosity in time, which in turn may be related  
540 to the observed explosive growth of large aggregates (> 5 mm). Together, these  
541 physical processes have a direct effect on particle size and sinking fluxes. They also  
542 influence the efficiency of the biological pump by increasing the residence times of  
543 particulate material in the upper layers, enabling more time for microbes and metazoans  
544 to remineralize and graze these particles. The net result of these competing processes  
545 will vary as a function of the coupling among food web, particle, and physical  
546 oceanographic dynamics, presenting a challenge for observing and modeling the  
547 mechanisms regulating important carbon cycling metrics, such as e-ratios and  
548 remineralization length scales.

549 We also show that biotic processes in the mesopelagic zone are disaggregating large (>  
550 0.5 mm) particles into smaller ones (< 0.5 mm). This is likely related to the abundance  
551 and activity of zooplankton as other sources of these smaller particles within the ECWs  
552 seems unlikely. These observations support recent studies suggesting that  
553 disaggregation processes are a critical component of flux attenuation with depth  
554 (Giering et al. 2014; 2023; Collins et al. 2015; Briggs et al. 2020). Biological  
555 disaggregation is thought to be an important, yet poorly represented, process in models  
556 of the biological pump (Iversen, 2023; Burd, 2024). Further, the production of small  
557 particles at depth provides a mechanism for their presence in sediment traps besides  
558 sinking from the sea surface (Richardson and Jackson, 2007). Thus, both abiotic and  
559 biotic particle aggregation and disaggregation processes need to be included in  
560 observational assessments and numerical models of the biological pump (Siegel et al.  
561 2023a; Burd, 2024).

562 The sampling design of the EXPORTS-NA study leveraged the retentive nature of an  
563 anticyclonic eddy to enable observations of coupled ecological / biogeochemical  
564 processes in as close to a Lagrangian fashion as possible. The present observations of  
565 the large particle distribution inside and outside of the eddy core waters demonstrated

566 that this goal was achieved, essentially separating temporal-vertical changes from  
567 lateral transport processes that would obscure signals of vertical export. This meant that  
568 the ECWs provided a near-pristine laboratory for us to understand the relationships  
569 among particle dynamics and sinking particles fluxes. In all, this work illustrates the  
570 importance of Lagrangian sampling designs to provide the required observational data  
571 for understanding the biological pump, particularly for sites with high eddy kinetic energy  
572 levels (Briggs et al. 2011; Siegel et al. 2016; Johnson et al. 2024).

573 Last, there is a great deal of interest in the development of ocean-based carbon dioxide  
574 reduction (CDR) strategies to reduce atmospheric CO<sub>2</sub> levels (NASEM, 2022).  
575 Measuring and validating the efficacy of a CDR action is critical for monetizing the  
576 carbon offsets its produces. Several biotic ocean CDR methods, such as ocean iron  
577 fertilization or artificial upwelling, attempt to intensify carbon export fluxes of the  
578 biological pump by spurring upper ocean NPP rates. Our work demonstrates that a  
579 complex combination of physical, biogeochemical and ecological processes will  
580 determine the fates of the enhanced carbon export and illustrates the complexity and  
581 challenges in monitoring and validating the additional carbon sequestered by the CDR  
582 action.

## 583 References:

- 584 Alldredge, A.L., C. Gotschalk, In situ settling behavior of marine snow. *Limnol. Oceanogr.*, **33**,  
585 339–351, (1988).
- 586 Alldredge, A.L., T.C. Granata, C.C. Gotschalk, T.D. Dickey, The physical strength of marine  
587 snow and its implications for particle disaggregation in the ocean. *Limnol. Oceanogr.*, **35**,  
588 1415-1428, (1990).
- 589 Behrenfeld, M.J., Abandoning Sverdrup's critical depth hypothesis on phytoplankton  
590 blooms. *Ecology*, **91**, 977-989, (2010).
- 591 Belcher, A., M. Iversen, S. Giering, V. Riou, S.A. Henson, L. Berline, L. Guilloux, R. Sanders,  
592 Depth-resolved particle-associated microbial respiration in the northeast Atlantic,  
593 *Biogeosciences*, **13**, 4927–4943, <https://doi.org/10.5194/bg-13-4927-2016>, (2016).
- 594 Briggs, N., M.J. Perry, I. Cetinić, C. Lee, E. D'Asaro, A.M. Gray, E. Rehm, High-resolution  
595 observations of aggregate flux during a sub-polar North Atlantic spring bloom. *Deep-Sea*  
596 *Res. Part I*, **58**, 1031-1039, (2011).
- 597 Briggs, N., G. Dall'Olmo, H. Claustre, Major role of particle fragmentation in regulating biological  
598 sequestration of CO<sub>2</sub> by the oceans. *Science*, **367**, 791-793, (2020).
- 599 Brzezinski, M.A., L. Johnson, M. Estapa, S. Clevenger, M. Roca-Martí, E. Romanelli, K.N. Buck,  
600 B.D. Jenkins and J.L. Jones, in review, Physical mechanisms sustaining silica production  
601 following the demise of the diatom phase of the North Atlantic spring phytoplankton bloom  
602 during EXPORTS. In review at *Global Biogeochemical Cycles*.
- 603 Buesseler, K.O., P.W. Boyd, E.E. Black, D.A. Siegel, Metrics that matter for assessing the  
604 ocean biological carbon pump. *Proc. Natl. Acad. Sci. U.S.A.*, **117**, 9679-9687, (2020).

605 Burd, A.B., Modeling the Vertical Flux of Organic Carbon in the Global Ocean. *Annual Review of*  
606 *Marine Science*, **16**, <https://doi.org/10.1146/annurev-marine-022123-102516>, (2024).

607 Burd, A.B. G.A. Jackson, Particle aggregation. *Annual Review of Marine Science*, **1**, 65-90,  
608 <https://doi.org/10.1146/annurev.marine.010908.163904>, (2009).

609 Cetinić, I., M.J. Perry, E. D'Asaro, N. Briggs, N. Poulton, M.E. Sieracki, C.M. Lee, A simple  
610 optical index shows spatial and temporal heterogeneity in phytoplankton community  
611 composition during the 2008 North Atlantic Bloom Experiment, *Biogeosciences*, **12**, 2179–  
612 2194, <https://doi.org/10.5194/bg-12-2179-2015>, (2015).

613 Collins, J.R., B.R. Edwards, K. Thamatrakoln, J.E. Ossolinski, G.R. DiTullio, K.D. Bidle, S.C.  
614 Doney, B.A. Van Mooy, The multiple fates of sinking particles in the North Atlantic  
615 Ocean. *Global Biogeochemical Cycles*, **29**, 1471-1494, (2015).

616 Clevenger S.J., C.R. Benitez-Nelson, M. Roca-Martí, W. Bam, M. Estapa, J.A. Kenyon, S. Pike,  
617 L. Resplandy, A. Wyatt, K.O. Buesseler, Carbon and silica fluxes during a declining North  
618 Atlantic spring bloom as part of the EXPORTS program. *Marine Chemistry* **258**, 104346.  
619 <https://doi.org/10.1016/j.marchem.2023.104346>, (2024).

620 Dall'Olmo, G., J. Dingle, L. Polimene, R.J. Brewin, H. Claustre, Substantial energy input to the  
621 mesopelagic ecosystem from the seasonal mixed-layer pump. *Nature Geoscience*, **9**, 820-  
622 823, (2016).

623 Dilling, L., A.L. Alldredge, Fragmentation of marine snow by swimming macrozooplankton: a  
624 new process impacting carbon cycling in the sea. *Deep-Sea Res. I*, **47**, 1227-1245, (2000).

625 Dilling, L., J. Wilson, D. Steinberg, A. Alldredge, Feeding by the euphausiid, *Euphausia pacifica*,  
626 and the copepod, *Calanus Pacificus*, on marine snow. *Mar. Ecol. Prog. Ser.*, **170**, 189-20.  
627 DOI: [10.3354/meps170189](https://doi.org/10.3354/meps170189), (1998).

628 Ducklow, H.W., D.K. Steinberg, K.O. Buesseler, Upper ocean carbon export and the biological  
629 pump. *Oceanography*, **14**, 50-58, (2001).

630 Ducklow, H.W., R.P. Harris, Introduction to the JGOFS North Atlantic bloom experiment. *Deep*  
631 *Sea Research Part II*, **40**, 1-8, (1993).

632 Durkin, C.A., M.L. Estapa, K.O. Buesseler, Observations of carbon export by small sinking  
633 particles in the upper mesopelagic. *Marine Chemistry*, **175**, 72-81, (2015).

634 Erickson, Z.K., E. Fields, L. Johnson, A.F. Thompson, L.A. Dove, E. D'Asaro, D.A. Siegel, Eddy  
635 tracking from in situ and satellite observations. *Journal of Geophysical Research: Oceans*,  
636 **128**, e2023JC019701. <https://doi.org/10.1029/2023JC019701>, (2023).

637 Estapa M.L., C.A. Durkin, W.H. Slade, C.L. Huffard, S.P. O'Neill, M.M. Omand, A new, global  
638 optical sediment trap calibration. *Limnology & Ocean Methods*: lom3.10592.  
639 <https://doi.org/10.1002/lom3.10592>, (2023).

640 Giering, S.L., R. Sanders, R.S. Lampitt, T.R. Anderson, C. Tamburini, M. Boutrif, M.V. Zubkov,  
641 C.M. Marsay, S.A. Henson, K. Saw, K. Cook, Reconciliation of the carbon budget in the  
642 ocean's twilight zone. *Nature*, **507**, 480-483, (2014).

643 Giering, S. L. C., R. Sanders, A.P. Martin, S.A. Henson, J.S. Riley, C.M. Marsay, D.G. Johns  
644 Particle flux in the oceans: Challenging the steady state assumption, *Global Biogeochemical*  
645 *Cycles*, **31**, 159–171, <https://doi.org/10.1002/2016GB005424>, (2017).

646 Giering, S.L.C., R. Sanders, S. Blackbird, N. Briggs, F. Carvalho, H. East, et al., Vertical  
647 imbalance in organic carbon budgets is indicative of a missing vertical transfer during a

648 phytoplankton bloom near South Georgia (COMICS). *Deep Sea Res. Part II*, **209**, 105277,  
649 (2023).

650 Goldthwait, S., J. Yen, J. Brown, A. Alldredge, Quantification of marine snow fragmentation by  
651 swimming euphausiids, *Limnology and Oceanography*, **49**, 940-952,  
652 <https://doi.org/10.4319/lo.2004.49.4.0940>, (2004).

653 Henson, S.A., Laufkötter, C., Leung, S. *et al.* Uncertain response of ocean biological carbon  
654 export in a changing world. *Nat. Geosci.* **15**, 248–254, <https://doi.org/10.1038/s41561-022-00927-0>, (2022).

656 Iversen, M.H., Carbon Export in the Ocean: A Biologist's Perspective. *Annual Review of Marine*  
657 *Science*, **15**, 357-381, <https://doi.org/10.1146/annurev-marine-032122-035153>, (2023).

658 Jackson G.A., A model of the formation of marine algal flocs by physical coagulation processes.  
659 *Deep-Sea Res. A* **37**, 1197–211, (1990).

660 Jackson, G.A., A.B. Burd, Simulating aggregate dynamics in ocean biogeochemical models.  
661 *Prog. Oceanog.*, **133**, 55–65, <https://doi.org/10.1016/j.pocean.2014.08.014>, (2015).

662 Johnson, L., D.A. Siegel, A.F. Thompson, E. Fields, Z.K. Erickson, I. Cetinić, I., *et al.*,  
663 Assessment of oceanographic conditions during the North Atlantic EXport processes in the  
664 ocean from RemoTe Sensing (EXPORTS) Field campaign. *Prog. Oceanog.*, 103170,  
665 <https://doi.org/10.1016/j.pocean.2023.103170>, (2024).

666 Kriest, I., Different parameterizations of marine snow in a 1D-model and their influence on  
667 representation of marine snow, nitrogen budget and sedimentation. *Deep Sea Res. Part I*,  
668 **49**, 2133-2162. (2002).

669 Laurenceau-Cornec, E.C., T.E. Trull, D.M. Davies, L. Christina, S. Blain, Phytoplankton  
670 morphology controls on marine snow sinking velocity. *Mar. Ecol. Prog. Ser.*, **520**, 35-56,  
671 (2015).

672 Laurenceau-Cornec E.C., M. Mongin, T.W. Trull, M. Bressac, E.L. Cavan, L.T. Bach, *et al.*,  
673 Concepts toward a global mechanistic mapping of ocean carbon export. *Global Biogeochem.*  
674 *Cyc.*, **37**, e2023GB007742. <https://doi.org/10.1029/2023GB007742>, (2023).

675 Le Moigne, F.A., Pathways of organic carbon downward transport by the oceanic biological  
676 carbon pump. *Frontiers in Marine Science*, **6**, 634, (2019).

677 Logan, B.E., D.B. Wilkinson, Fractal geometry of marine snow and other biological aggregates.  
678 *Limnol. Oceanogr.* **35**, 130–136. doi:10.2307/2837345, (1990).

679 Mahadevan, A., E. D'Asaro, C. Lee, M.J. Perry, Eddy-driven stratification initiates North Atlantic  
680 spring phytoplankton blooms. *Science*, **337**, 54-58 (2012).

681 Meyer, M.G., Brzezinski, M., Cohn, M.R., Kramer, S.J., Paul, N., Sharpe, G.C., *et al.*, Primary  
682 production dynamics during the decline phase of the North Atlantic annual spring  
683 bloom. *bioRxiv*, <https://doi.org/10.1101/2023.05.18.541304>, (2023).

684 Møller, E.F., P. Thor, T.G. Nielsen, Production of DOC by *Calanus finmarchicus*, *C. glacialis*  
685 and *C. hyperboreus* through sloppy feeding and leakage from fecal pellets. *Mar. Ecol. Prog.*  
686 *Ser.*, 262, 185–191, (2003).

687 National Academies of Sciences, Engineering, and Medicine. *A Research Strategy for Ocean-*  
688 *based Carbon Dioxide Removal and Sequestration*. Washington, DC: The National  
689 Academies Press. <https://doi.org/10.17226/26278>, (2022).



690 Nowicki, M., T. DeVries, and D.A. Siegel, Quantifying the carbon export and sequestration  
691 pathways of the ocean's biological carbon pump. *Global Biogeochemical Cycles*,  
692 <https://doi.org/10.1029/2021GB007083>, (2022).

693 Picheral, M., L. Guidi, L. Stemann, D.M. Karl, G. Iddaoud, G. Gorsky, The Underwater Vision  
694 Profiler 5: An advanced instrument for high spatial resolution studies of particle size spectra  
695 and zooplankton. *Limnol. Oceanogr.: Methods*, **8**, 462-473, (2010).

696 Richardson T.L., G.A. Jackson, Small phytoplankton and carbon export from the surface ocean.  
697 *Science*, 315, 838-840, <https://doi.org/10.1126/science.1133471>. (2007).

698 Romanelli, E., S.L.C. Giering, M. Estapa, D.A. Siegel, U. Passow, Intense storms affect sinking  
699 particle fluxes after the North Atlantic diatom spring bloom. bioRxiv 2024.01.11.575202;  
700 <https://doi.org/10.1101/2024.01.11.575202>, (2024).

701 Siegel, D.A., S.C. Doney and J.A. Yoder, The North Atlantic spring phytoplankton bloom in the  
702 and Sverdrup's critical depth hypothesis. *Science*, **296**, 730-733.  
703 <https://doi.org/10.1126/science.1069174>, (2002).

704 Siegel, D. A., Buesseler, K. O., Behrenfeld, M. J., Benitez-Nelson, C. R., Boss, E., Brzezinski,  
705 M. A., et al., Prediction of the export and fate of global ocean net primary production: The  
706 EXPORTS science plan. *Frontiers in Marine Science*, **3**,  
707 <https://doi.org/10.3389/fmars.2016.00022>, (2016).

708 Siegel, D.A., T. DeVries, I. Cetinić, K.M. Bisson, Quantifying the Ocean's Biological Pump and  
709 its Carbon Cycle Impacts on Global Scales. *Annual Review of Marine Sciences*.  
710 <https://doi.org/10.1146/annurev-marine-040722-115226>, (2023a).

711 Sieracki, M.E., P.G. Verity, D.K. Stoecker, Plankton community response to sequential silicate  
712 and nitrate depletion during the 1989 North Atlantic spring bloom. *Deep Sea Research Part*  
713 *II*, **40**, 213-225, (1993).

714 Song Y., A.B. Burd, M.J. Rau, The deformation of marine snow enables its disaggregation in  
715 simulated oceanic shear. *Front. Mar. Sci.* 10:1224518,  
716 <https://doi.org/10.3389/fmars.2023.1224518>, (2023).

717 Steinberg, D.K., M.R. Landry, Zooplankton and the ocean carbon cycle. *Annual Review of*  
718 *Marine Sciences*, **9**, 413-444, (2017).

719 Stemann, L., Jackson, G.A. and Ianson, D., A vertical model of particle size distributions and  
720 fluxes in the midwater column that includes biological and physical processes—Part I: model  
721 formulation. *Deep Sea Research Part I*: **51**, 865-884,  
722 <https://doi.org/10.1016/j.dsr.2004.03.001>, (2004).

723 Sverdrup, H.U., On conditions for the vernal blooming of phytoplankton. *J. Cons. Int. Explor.*  
724 *Mer*, **18**, 287-295, (1953).

725 Takeuchi, M., M.J. Doubell, G.A. Jackson, Turbulence mediates marine aggregate formation  
726 and destruction in the upper ocean. *Sci Rep* **9**, 16280, [https://doi.org/10.1038/s41598-019-](https://doi.org/10.1038/s41598-019-52470-5)  
727 [52470-5](https://doi.org/10.1038/s41598-019-52470-5), (2019).

728 Uitz, J., H. Claustre, A. Morel, S.B. Hooker, Vertical distribution of phytoplankton communities in  
729 open ocean: An assessment based on surface chlorophyll. *Journal of Geophysical*  
730 *Research*, 111(C08005), 1–23. <https://doi.org/10.1029/2005JC003207>, (2006).

731 Wassmann, P., Retention versus export food chains: processes controlling sinking loss from  
732 marine pelagic systems. *Hydrobiologia* **363**: 29–57, (1998).



734 **Methods:**

735 Experimental Array and Siting: The EXPORTS-NA field campaign was conducted ~150 km due  
736 east of the Porcupine Abyssal Plain (PAP) Observatory (Hartman et al. 2021) in the northeast  
737 Atlantic Ocean within anticyclone eddy (Fig. S1; Erickson et al. 2023; Johnson et al. 2024).  
738 Three research vessels (RRS *James Cook*, RRS *Discovery* & R/V *Sarmiento de Gamboa*),  
739 three instrumented gliders, an instrumented Lagrangian float and 10 water following surface  
740 drifters were deployed during the experiment. The location of the eddy center was monitored by  
741 analyzing available horizontal velocity measurements from the multiple sampling assets and  
742 verified by the instrumented Lagrangian float that was deployed near the eddy center at depth of  
743 ~90 m (Erickson et al. 2023). Measurements within 15 km of the analyzed eddy center were  
744 deemed in the eddy core based upon water property analyses. Below about 120 m, in the eddy  
745 core waters (ECWs), water parcels were retained within the eddy throughout the experiment  
746 (Johnson et al. 2024). Thus, changes in biogeochemical and ecological properties in the ECWs  
747 were due to local processes and were independent of changes due to horizontal advection.  
748 However, in the surface core waters (SCWs) above the eddy, a series of four intense storms  
749 interrupted ship-based sampling (Fig. S1), deepened mixed layer depths and exchanged  
750 significant fractions of the upper water column (roughly 25 to 75%) due to Ekman transport  
751 (Johnson et al. 2024).

752 Measurement Protocols: Measurement protocols for all measurements made during EXPORTS  
753 are available at <https://sites.google.com/view/oceanexports>. This includes the context variables  
754 presented in Fig. 1 for phytoplankton pigments, POC, and bSi concentrations, as well as 14-C  
755 NPP and sediment trap export fluxes.

756 Characterizing Large Particles using In Situ Imagery: Abundance and size of large particles and  
757 aggregates were quantified as a function of depth using the Underwater Vision Profiler 5 (UVP;  
758 Picheral et al. 2010) deployed from each of the three research vessels. The UVP illuminates  
759 approximately 1 L of seawater imaged at a pixel resolution of ~50  $\mu\text{m}$ . Particles are identified as  
760 contiguous pixels whose area is converted equivalent spherical diameter. Particle abundance  
761 size distributions are then calculated for 25 logarithmically distribution bins with center bin  
762 diameters ranging from 0.09 to 23.9 mm. In standardizing the UVP data from the three ships,  
763 the first two bins were removed from consideration, making 0.13 mm the smallest particle  
764 diameter bin center reliably imaged (Siegel et al. 2023b). Particle abundance size distributions  
765 are averaged into 5 m vertical bins for equivalent spherical diameters ranging from 0.13 to 10  
766 mm. Given the UVP's sampling frequency (6 Hz) and typical CTD frame lowering rates, nearly  
767 100 individual scans make up each 5-m vertical average. This corresponds to each 5 m bin  
768 sampling ~ 100 L of seawater. Particle size spectra are reported here as particle volume spectra  
769 in differential form (units are ppmV per mm bin width) as they accentuate changes in the particle  
770 size spectra compared to visualizations made with particle abundance spectra and do not  
771 require the simultaneous reporting of bin dimensions (Jackson et al. 1997; Zhang et al. 2023).  
772 Further details including the standardizing of UVP particle size distribution data from the three  
773 ships is included in Siegel et al. (2023b).

774 Total particle volumes are calculated as the integral of the differential particle volume spectra  
775 over the range of available diameters. Vertical sinking flux for particles is calculated as the

776 integral of the daily mean differential particle volume spectra multiplied by an assumed sinking  
777 speed distribution over the diameters considered. Here, a theoretical sinking speed distribution  
778 from Kriest (2002) is used (their ref 8 in Table 2; the lower of the two curves presented in Fig.  
779 2c). The size of the largest particles robustly sampled,  $D_{\max}$ , is quantified as the largest  
780 differential particle volume threshold value that that is consistently well sampled by the UVP. A  
781 threshold value of 4 ppmV/mm provided consistent assessment of  $D_{\max}$  for the mixed layer via  
782 experimentation with different thresholds.

783 Sinking speed size distributions were estimated from particle abundance distributions following  
784 Lacour et al. (2023). For each size bin, particle abundance time-depth distributions were first  
785 smoothed and then 6 to 10 particle abundance isosurfaces are selected. The mean and  
786 standard deviation of the slope determinations of the depth-time relationships for the period May  
787 14 to 25 are then calculated. Bin centers used range from 0.11 to 3.65 mm.

788 Aggregates abundances were quantified from an analysis of thumbnail images of large  
789 individual objects ( $> 1$  mm). This classification was conducted first by using MorphoCluster  
790 (Schröder et al. 2020), which enables the fast, human-assisted assimilation of likewise-  
791 appearing objects into clusters and subsequent classification. Thumbnails and their  
792 classification were uploaded to EcoTaxa (<https://ecotaxa.obs-vlfr.fr>) where classifications were  
793 further checked. Abundances of "fluffy" and "very fluffy" aggregates classified in this manner  
794 were binned together into 5 m vertical bins and daily averages (Drago et al. in prep.).

795 Sediment Trap Estimates of Sinking Particle Composition, Mass and Volume Fluxes: Surface-  
796 tethered and neutrally-buoyant arrays of sediment traps were deployed three times during the  
797 cruise as described by Estapa et al. (2021; 2023). Cylindrical trap tubes ( $0.0113 \text{ m}^2$ ) carried  
798 either poisoned brine (for bulk measurements of sinking POC, PIC, bSi, and mass flux) or  
799 polyacrylamide gel collectors (Durkin et al., 2021) for particle enumeration, size, and  
800 classification. POC flux was determined following Estapa et al. (2023). PIC flux was measured  
801 by coulometric analysis (Honjo et al., 2000) on gravimetric splits of the same filters used for  
802 POC. Biogenic silica was measured by hot alkaline extraction of sample splits filtered onto  
803 polycarbonate membranes followed by spectrophotometric analysis (Brzezinski et al., *in review*).  
804 Gels were digitally imaged at 7x, 32x, and 115x magnification, then particles were identified and  
805 enumerated following methods similar to Durkin et al. (2021). Image pixel size at 32x resolution  
806 was intercalibrated with the pixel size at 7x resolution following Jackson et al. (1997). Particle  
807 diameter was used to estimate volume, assuming particles were spheres. Volume and mass  
808 fluxes were finally calculated by normalizing to trap deployment length and collection area.  
809 Surface tethered traps were subjected to horizontal velocities exceeding  $30 \text{ cm s}^{-1}$  and the  
810 upper trap briefly was within the surface mixed layer during Epoch 3, so only data from  
811 neutrally-buoyant sediment traps are shown in that Epoch.

812 Marine Snow Catcher Assessments of Aggregate Abundances and POC Fluxes: Sinking  
813 particles and sinking aggregates (ESD  $> 0.1$  mm) were collected below the mixed layer down to  
814 depths of 500 m using four Marine Snow Catchers (MSC) as detailed by Romanelli et al. (2023).  
815 After retrieval, each MSC was placed on deck in an upright position for exactly 2 hours to allow  
816 the sinking of aggregates inside a circular plastic tray placed inside the base section of the  
817 MSC. Right after, the water collected in the base overlying the tray was gently sampled and the  
818 tray was transferred to the lab to manually pick individual aggregates (Romanelli et al., 2024).  
819 The aggregates were visually sized and counted. On May 27, the POC mass of the sinking  
820 aggregates was measured and used to calculate the POC concentration associated with the

821 sinking aggregates (Romanelli et al., 2024). The base water and tray water (without the sinking  
 822 aggregates) were processed to assess the POC concentrations of sinking particles. The sinking  
 823 velocity of the entire sinking particle population (i.e., sinking particles plus sinking aggregates)  
 824 was calculated by dividing the POC fluxes obtained from co-deployed sediment traps to the  
 825 POC concentration of sinking particles collected with the MSCs (Romanelli et al., 2024). Particle  
 826 fluxes were calculated by multiplying the concentration of sinking particles by an estimate of  
 827 their average sinking velocity.

828 Assessments of Solid Fractions of Sinking and Suspended Particles: Particle solid fractions  
 829 were estimated as the ratio of solid particle component volumes to total particle volume. For  
 830 sinking particles, measurements of bulk fluxes of POC, biogenic silica (bSi), and particulate  
 831 inorganic carbon (PIC) (described above) were used to estimate the mass fluxes of organic  
 832 matter, opal, and calcium carbonate, and representative component densities were then used to  
 833 estimate the volume flux of the solid fraction in the particles (POC to organic matter: Lam et al.  
 834 2011; bSi to opal: Mortlock and Froelich, 1989; PIC to CaCO<sub>3</sub>: stoichiometry; densities:  
 835 Laurenceau-Cornec et al., 2020). For suspended particles, a similar process was used to  
 836 estimate the solid volume concentration from POC, bSi, and PIC concentrations measured in  
 837 the > 335 μm size fraction of the large volume pump samples (Clevenger et al. 2024). For  
 838 sinking particles, the total particle volume flux was estimated as described above, while for  
 839 suspended particles, the volume concentration of ≥ 335 μm particles was estimated from UVP  
 840 images. For both suspended and sinking particles, solid fractions were determined by dividing  
 841 the corresponding solid volume by the total volume.

842 Estimation of Turbulent Kinetic Dissipation Rates from Air-Sea Flux Determinations: Turbulent  
 843 kinetic energy dissipation rates ( $KE_{diss}$ ;  $W\ kg^{-1}$ ) were calculated for the upper 50 m of the water  
 844 column using established similarity scalings described by Lombardo and Gregg (1989) and  
 845 D'Asaro (2014), or

$$846 \quad KE_{diss} = 0.58 \left( -\frac{g\alpha Q}{\rho_o c_p} + g\beta(E - P)S_o \right) + \frac{1.76(\tau/\rho_o)^{3/2}}{\kappa z} \quad (M1)$$

847 The first term represents the contribution from surface buoyancy forcing, where  $g$  is gravity,  $\alpha$  is  
 848 the thermal expansion coefficient,  $Q$  is the surface net heat flux,  $\rho_o$  is a reference density,  $\beta$  is  
 849 the haline contraction coefficient,  $E$  is evaporation,  $P$  is precipitation and  $S_o$  is a reference  
 850 salinity. The second term represents the contribution from momentum input, where  $\tau$  is the  
 851 surface wind stress,  $\kappa$  is the von Karmen constant, and  $z$  is depth from the surface. Surface  
 852 heat and freshwater fluxes and wind stress were estimated using ship based meteorological  
 853 measurements processed with the COARE bulk formula. Additional details can be found in  
 854 Johnson et al. (2024).

855 Modeling of Particle Coagulation and Disaggregation Rates: Particle coagulation rates are  
 856 calculated using standard coagulation theory with a turbulent shear coagulation curvilinear  
 857 kernel (Burd and Jackson, 2009) using turbulent kinetic energy dissipation rates determined  
 858 above. Particle coagulation rates are calculated from the coagulation equations using a size-  
 859 class based discretization from which total formation rates of large particles by coagulation are  
 860 calculated (Burd, 2013). The UVP-determined ESD volume distributions are converted to  
 861 conserved volumes ensuring total particle numbers remained the same (Jackson, 1990). Large  
 862 uncertainties exist for the fractal dimensions used for this conversion. Thus, an ensemble of  
 863 simulations was created using a range of particle fractal dimensions from 1.5 to 2.3 covering a

864 range of values from the literature (Logan and Alldredge 1989; Li and Logan 1995; Risović and  
865 Martinis 1996; Jackson et al. 1997; Ploug et al. 2008). The ensemble included both particle  
866 fractal dimensions that are constant in time as well as examples that linearly decrease in time  
867 with initial and final values chosen randomly from above range. The final ensemble was made  
868 up of 21 members. Means and standard deviations of large particle formation rates by  
869 coagulation are calculated from the ensemble and shown in Figs. 3e and 5b.

870 Disaggregation rates of large particles are calculated following the model of Alldredge et al.  
871 (1990). Maximum particle sizes are calculated as  $D_{\max} = 0.75 (KE_{\text{diss}})^{-0.15}$ . Conserved particle  
872 volumes in aggregates larger than  $D_{\max}$  are redistributed into smaller particles such that 2/3 of  
873 the volume goes into the next size class smaller than the maximum particle size and the  
874 remaining volume is distributed uniformly among the smaller size classes.

875 Rates of large particle (> 5 mm) formation due to differential sedimentation were also  
876 determined (Burd and Jackson, 2009). Conserved particle volume spectra were calculated as  
877 detailed above and particle sinking speed was calculated using Equation 8 of Table 2 in Kriest  
878 (2002) (the lower estimate in Fig. 2c). We find, for the 40 to 80 m layer where differential  
879 settlement should be more important, that shear coagulation rates are more than twelve times  
880 greater than differential sedimentation rates (Fig. S5). Hence, only rates of large particle  
881 formation due to shear coagulation are used in the qualitative discussions in the text.

882 Optical Sediment Trap and SnoCAM Sinking Particle Flux Determinations: Sinking particle  
883 fluxes were estimated at 75 m using two prototype tools for optical measurement of sinking  
884 particle fluxes that were both mounted on the instrumented Lagrangian Float deployed in the  
885 eddy core. A 25 cm beam transmissometer (~8 mm diameter collection area, C-Star, Sea-Bird  
886 Scientific Inc., Bellevue, WA) was used as an optical sediment trap as described by Estapa et  
887 al. (2023) and collected data at an hourly frequency. A prototype upward-facing time-lapse  
888 camera (5 cm diameter collection area, SnoCam, University of Rhode Island) collected images  
889 of sedimenting particles at 4 hour intervals. For both instruments, particle flux was determined  
890 from the rate of signal increase over time. For the transmissometer-OST, POC flux was  
891 empirically estimated from beam attenuation flux following Estapa et al. (2023). The SnoCam  
892 flux was reported as the rate of increase of particle projected area ( $\text{mm}^2 \text{m}^{-2} \text{d}^{-1}$ ). The SnoCam  
893 imager was not optimized for sharp edge definition of porous, low fractal-dimension particles.

894 Radiochemical Assessment of POC Fluxes: Radiochemical assessment of POC fluxes via  $^{234}\text{Th}$   
895 measurements was carried out in accordance with the protocol described in Clevenger et al.  
896 (2021), wherein 2L seawater samples are precipitated with a  $\text{MnO}_2$  coprecipitation method.  
897 Low-level beta decay activity (counts per minute) are then determined via counting on anti-  
898 coincidence beta decay counters (Risø DTU National Laboratory, Denmark). Thorium-234  
899 fluxes ( $\text{dpm m}^{-2} \text{d}^{-1}$ ; dpm = decays per minute) were analyzed using a non-steady state model,  
900 detailed in Clevenger et al. (2024). The non-steady state model assumes that the study system  
901 changes on a timescale less than the half-life of  $^{234}\text{Th}$  (24.1 d). Thorium-234 fluxes were  
902 converted into POC fluxes by multiplying isotope fluxes by  $\text{POC}/^{234}\text{Th}$  ratios, collected using *in*  
903 *situ* pumps (McLane Labs), again detailed in Clevenger et al. (2024). Notably, POC fluxes  
904 included in this study are derived from the > 5  $\mu\text{m}$  particle size class.

905 Large Particle-Zooplankton Encounter Rates: Encounter rates between zooplankton and large  
906 particles are estimated using a simple, geometric encounter rate. Zooplankton abundance  
907 ( $\text{individuals m}^{-3}$ ) in 9 discrete depth intervals spanning 0-1000 m are calculated from MOCNESS

908 net tows (three day-night pairs on May 11, 17, and 26) conducted in the eddy core. At sea  
909 samples from each depth interval were split using a Folsom plankton splitter and processed  
910 using protocols described in Steinberg et al. (2008, 2023). Half of the sample was size-  
911 fractionated using nested sieves (200, 500, 1000, 2000, and 5000  $\mu\text{m}$ ), rinsed onto pre-weighed  
912 0.2 mm Nitex mesh filters, and frozen at  $-20^{\circ}\text{C}$  for dry biomass analysis. The dry weight  
913 biomass of each size fraction for each depth interval ( $\text{mg m}^{-3}$ ) was determined by dividing the  
914 biomass by the seawater volume filtered through the net. For the May 17th day-night pair, the  
915 other half of the sample was size-fractionated using the same nested sieves then preserved in  
916 sodium borate-buffered 4% formaldehyde. These preserved samples were imaged with a  
917 ZooSCAN version 3 at 2400 dpi as described in Maas et al. (2021). Briefly, at least 1500  
918 particles per size fraction were scanned after subsampling using a Motoda splitter (Motoda,  
919 1959). Raw images were processed in ZooProcess (Gorsky et al., 2010, Vandromme et al.,  
920 2012), then uploaded to EcoTaxa (<https://ecotaxa.obs-vlfr.fr/>; Picheral et al., 2017) for machine  
921 assisted identification and then manually validated. This dataset provides the abundance of  
922 zooplankton from each size fraction from each depth interval after accounting for fraction  
923 imaged and volume filtered. By dividing measured dry mass from the equivalent sample by this  
924 measured abundance, we can calculate the average size of a zooplankton in that size fraction  
925 and net. We assumed the same average size organisms for the May 11 and 26 day-night pairs  
926 to calculate zooplankton abundance from these tows.

927 Encounter rates are estimated assuming zooplankton within each depth interval are uniformly  
928 distributed using large particle abundances from the UVP and particle sinking speeds from Fig.  
929 1c. The encounter cross section between zooplankton and large particles is assumed to be 1  
930 mm to take into account hydromechanical signal detection of particles by zooplankton (Visser,  
931 2001).

932 Inverse Modeling Biotic Transformations of Small & Large Particles in the Mesopelagic: A  
933 simple inverse model (eq. 1) is used to assess the rates of transformation of large and small  
934 particle abundances in the mesopelagic via linear regression. The UVP-determined ESD  
935 volume distributions are converted to conserved volumes following methods detailed previously.  
936 Mean values and gradients over both depth and time are then calculated using the daily mean  
937 observations of the small and large conserved volumes for six temporal intervals spanning  
938 different portions of the experiment and four 50 m vertical intervals. Linear regression analysis is  
939 then applied to estimate the four parameters in the inverse model. This is repeated for each  
940 member of the ensemble and uncertainties are assessed as the standard deviation of the  
941 ensemble of retrievals.

942 **Methods References** (only those references not included in the main text):

- 943 Burd, A.B., Modeling particle aggregation using size class and size spectrum approaches. *J.*  
944 *Geophys. Res. Oceans*, **118**, 3431–3443, <https://doi.org/10.1002/jgrc.20255>, (2013).
- 945 Clevenger S.J., C.R. Benitez-Nelson, J. Drysdale S. Pike, V. Puigcorb , K.O. Buesseler,  
946 Review of the analysis of  $^{234}\text{Th}$  in small volume (2-4L) seawater samples: improvements and  
947 recommendations. *J. Radioanal. Nucl. Chem.* **329**, 1-13, (2021).
- 948 D'Asaro, E.A., Turbulence in the upper-ocean mixed layer. *Annual Review of Marine Science*, **6**,  
949 101-115, (2014).

950 Drago, L., K. Buesseler, L. Karp-Boss, A.M.P. McDonnell, S.-M. Schröder, D.A. Siegel, L.  
951 Stemmann and R. Kiko, North Atlantic biological pump dynamics in an anticyclonic eddy  
952 revealed via in situ imaging, in prep.

953 Durkin C.A., K.O. Buesseler, I. Cetinić, M.L. Estapa, R.P. Kelly, M. Omand, A visual tour of  
954 carbon export by sinking particles. *Global Biogeochemical Cycles*, **35**, e2021GB006985.  
955 <https://doi.org/10.1029/2021GB006985>, (2021).

956 Estapa ML, Buesseler K, Durkin CA, Omand M, Benitez-Nelson CR, Roca-Martí M, Breves E,  
957 Kelly RP, Pike S. Biogenic sinking particle fluxes and sediment trap collection efficiency at  
958 Ocean Station Papa. *Elementa: Science of the Anthropocene*, **9**, 00122. doi:  
959 10.1525/elementa.2020.00122, (2021).

960 Gorsky, G., M. D. Ohman, M. Picheral, S. Gasparini, L. Stemmann, J-B Romagnan, A.  
961 Cawood, S. Pesant, C. García-Comas, and F. Prejger . 2010. Digital zooplankton image  
962 analysis using the ZooScan integrated system. *J. Plankt. Res.* **32**, 285-303.  
963 <https://doi.org/10.1093/plankt/fbp124>, (2010).

964 Hartman, S.E., Bett, B.J., Durden, J.M., Henson, S.A., Iversen, M., Jeffreys, R.M., Horton, T.,  
965 Lampitt, R. and Gates, A.R., Enduring science: three decades of observing the Northeast  
966 Atlantic from the Porcupine Abyssal Plain Sustained Observatory (PAP-SO). *Progress in*  
967 *Oceanography*, **191**, <https://doi.org/10.1016/j.pocean.2020.102508>, (2021).

968 Honjo S., R. Francois, S. Manganini, J. Dymond, R. Collier, Particle fluxes to the interior of the  
969 Southern Ocean in the Western Pacific sector along 170.3W. *Deep Sea Research Part II*, **47**:  
970 3521–3548, (2000).

971 Jackson, G.A., A model of the formation of marine algal flocs by physical coagulation  
972 processes. *Deep-Sea Res. A* **37**:1197–211, (1990).

973 Jackson, G.A., R. Maffione, D.K. Costello, A.L. Alldredge, B.E. Logan, H.G. Dam, Particle size  
974 spectra between 1 µm and 1 cm at Monterey Bay determined using multiple instruments.  
975 *Deep-Sea Research I*, 44:1739–1767, (1997).

976 Lacour, L., Llorc, J., Briggs, N., Strutton, P.G. and Boyd, P.W., Seasonality of downward carbon  
977 export in the Pacific Southern Ocean revealed by multi-year robotic observations. *Nature*  
978 *Communications*, **14**, p.1278, <https://www.nature.com/articles/s41467-023-36954-7>, (2023).

979 Lam P.J., S.C. Doney, J.K.B. Bishop, The dynamic ocean biological pump: Insights from a  
980 global compilation of particulate organic carbon, CaCO<sub>3</sub>, and opal concentration profiles from  
981 the mesopelagic. *Global Biogeochemical Cycles* 25(3). doi: 10.1029/2010GB003868, (2011).

982 Laurenceau-Cornec, E.C., Le Moigne, F.A., Gallinari, M., Moriceau, B., Toullec, J., Iversen,  
983 M.H., Engel, A. and De La Rocha, C.L., New guidelines for the application of Stokes' models  
984 to the sinking velocity of marine aggregates. *Limnology and Oceanography*, 65(6), pp.1264-  
985 1285. <https://doi.org/10.1002/lno.11388>, (2020).

986 Li, X., B.E. Logan, Size distributions and fractal properties of particles during a simulated  
987 phytoplankton bloom in a mesocosm. *Deep-Sea Research II*, 42:125–138, (1995).

988 Logan, BE, A.L. Alldredge, The increased potential for nutrient uptake by flocculating diatoms.  
989 *Marine Biology*, **101**, 443–450, (1989).

990 Lombardo, C.P., M.C. Gregg, Similarity scaling of viscous and thermal dissipation in a  
991 convecting surface boundary layer. *Journal of Geophysical Research: Oceans*, 94(C5), 6273-  
992 6284, (1989).



- 993 Maas, A.E., A. Miccoli, K.S. Stamieszkin, C.A. Carlson, D.K. Steinberg, Allometry and the  
 994 calculation of zooplankton metabolism in the subarctic Northeast Pacific Ocean. *Journal of*  
 995 *Plankton Research*, **43**, 413–427, [doi: 10.1093/plankt/fbab026](https://doi.org/10.1093/plankt/fbab026), (2021).
- 996 Maas A.E., H. Gossner, M.J. Smith, L. Blanco-Bercial, Use of optical imaging datasets to  
 997 assess biogeochemical contributions of the mesozooplankton. *Journal of Plankton Research*,  
 998 **43**, 475–491, (2021).
- 999 Mortlock R.A., P.N. Froelich, A simple method for the rapid determination of biogenic opal in  
 1000 pelagic marine sediments. *Deep Sea Research Part A Oceanographic Research Papers*  
 1001 **36**(9): 1415–1426. doi: 10.1016/0198-0149(89)90092-7, (1989).
- 1002 Motoda, S., Devices of simple plankton apparatus. Memoirs of the Faculty of Fisheries  
 1003 Hokkaido University 7: 73-94, (1959).
- 1004 Picheral, M., S. Colin, J.O. Irisson. EcoTaxa, a tool for the taxonomic classification of  
 1005 images. <https://ecotaxa.obs-vlfr.fr/>, (2017).
- 1006 Ploug, H., M.H. Iversen, G. Fischer G., Ballast, sinking velocity, and apparent diffusivity within  
 1007 marine snow and fecal pellets: Implications for substrate turnover by attached bacteria.  
 1008 *Limnology and Oceanography*, **53**:1878–1886, (2008).
- 1009 Risović, D., M. Martinis, Fractal dimension of suspended particles in seawater. *Journal of*  
 1010 *Colloid and Interface Science*, **182**,199–203, (1996).
- 1011 Romanelli, E., J. Sweet, S.L.C. Giering, D.A. Siegel, U. Passow, The importance of transparent  
 1012 exopolymer particles over ballast in determining both sinking and suspension of small  
 1013 particles during late summer in the Northeast Pacific Ocean. *Elementa: Science of the*  
 1014 *Anthropocene*, **11**, 00122. <https://doi.org/10.1525/elementa.2022.00122>, (2023).
- 1015 Schröder, S.M., Kiko, R. and Koch, R., 2020. MorphoCluster: Efficient annotation of plankton  
 1016 images by clustering. *Sensors*, **20**, 3060. <https://doi.org/10.3390/s20113060>, (2020).
- 1017 Siegel, D.A., I. Cetinić, A.F. Thompson, N.B. Nelson, M. Sten, M. Omand, S. Traylor, D.  
 1018 Nicholson, E. D’Asaro, X. Zhang, Z.K. Erickson, L. Johnson, and I.M. Soto Ramos, EXport  
 1019 Processes in the Ocean from RemoTe Sensing (EXPORTS) North Atlantic sensor calibration  
 1020 and intercalibration documents. <https://doi.org/10.1575/1912/66998>, (2023b).
- 1021 Steinberg, D. K., Stamieszkin, K., Maas, A. E., Durkin, C. A., Passow, U., Estapa, M. L., et al.,  
 1022 The outsized role of salps in carbon export in the subarctic Northeast Pacific Ocean. *Global*  
 1023 *Biogeochemical Cycles*, **37**, e2022GB007523. <https://doi.org/10.1029/2022GB007523>,  
 1024 (2023).
- 1025 Steinberg, D. K., J. S. Cope, S. E. Wilson, and T. Kobari (2008) A comparison of mesopelagic  
 1026 mesozooplankton community structure in the subtropical and subarctic North Pacific Ocean.  
 1027 *Deep-Sea Research II* **55**(14-15): 1615-1635. <https://doi.org/10.1016/j.dsr2.2008.04.025>.
- 1028 Vandromme, P. L. Stemmann, C. García-Comas, L. Berline, G. Gorsky, Assessing biases in  
 1029 computing size spectra of automatically classified zooplankton from imaging systems: A case  
 1030 study with the ZooScan integrated system. *Methods in Oceanography*. 1-2. 3-21.  
 1031 <https://doi.org/10.1016/j.mio.2012.06.001>, (2012).
- 1032 Visser, A., 2001, Hydromechanical signals in the plankton. *Marine Ecology Progress Series*,  
 1033 **222**:1–24.
- 1034 Zhang, X. Y. Huot, D. Gray, H.M. Sosik, D. Siegel, L. Hu, et al., Particle size distribution at  
 1035 Ocean Station Papa from nanometers to millimeters constrained with intercomparison of

1036 seven methods. *Elementa: Science of the Anthropocene*; 11 (1): 00094.  
1037 <https://doi.org/10.1525/elementa.2022.00094>, (2023).

1038  
1039

1040 **Acknowledgements:**

1041 We would like to acknowledge support from the NASA Ocean Biology and  
1042 Biogeochemistry program, the National Science Foundation Biological and Chemical  
1043 Oceanography programs and the Woods Hole Oceanographic Institution's Ocean  
1044 Twilight Zone study. We greatly acknowledge the cooperation, skill and commitment of  
1045 the Captains, Crews, Research Technicians and Administrative Staffs of the RRS  
1046 James Cook (JC214), RRS Discovery (DY130 & DY131) and the R/V Sarmiento de  
1047 Gamboa (SG2105) for making the EXPORTS-NA field deployment a reality. Special  
1048 thanks to Laura Lorenzoni (NASA HQ), Mike Sieracki (formally NSF BIO-OCE), Paula  
1049 Bontempi (formally NASA HQ), and Quincy Allison and his team (ESPO - NASA AMES)  
1050 for their vision and support throughout the development and implementation of the  
1051 EXPORTS field campaign. Last, we like to thank our many EXPORTS colleagues for  
1052 their brilliance, dedication, hard work, support, and collegiality.

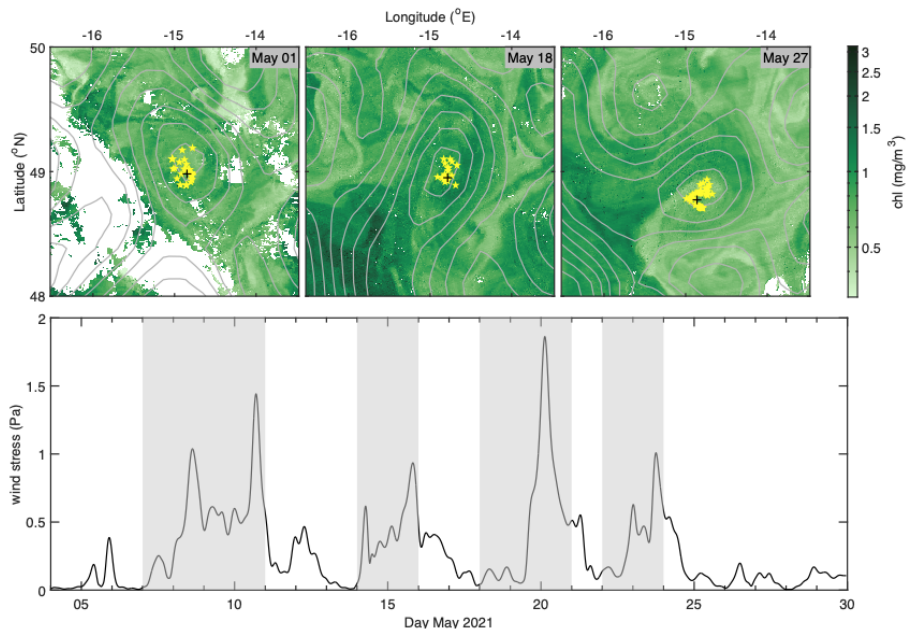
1053 **Data Availability:**

1054 All EXPORTS data used here is archived at NASA's SeaWiFS Bio-optical Archive and  
1055 Storage System (SeaBASS) under the EXPORTS Experiment  
1056 (<https://seabass.gsfc.nasa.gov/experiment/EXPORTS>). Data collected during the  
1057 EXPORTSNA field expedition onboard the Sarmiento the Gamboa was archived under  
1058 the OTZ\_WHOI experiment (10.5067/SeaBASS/OTZ\_WHOI/DATA001) and cruise  
1059 name SG2105. To find information about all the data collected under EXPORTS and  
1060 their data repositories and availability, please  
1061 visit: <https://sites.google.com/view/oceanexports/home>.



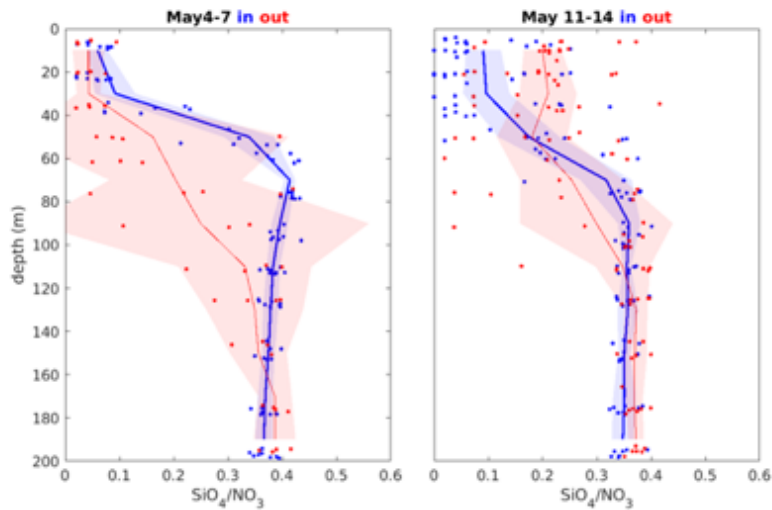
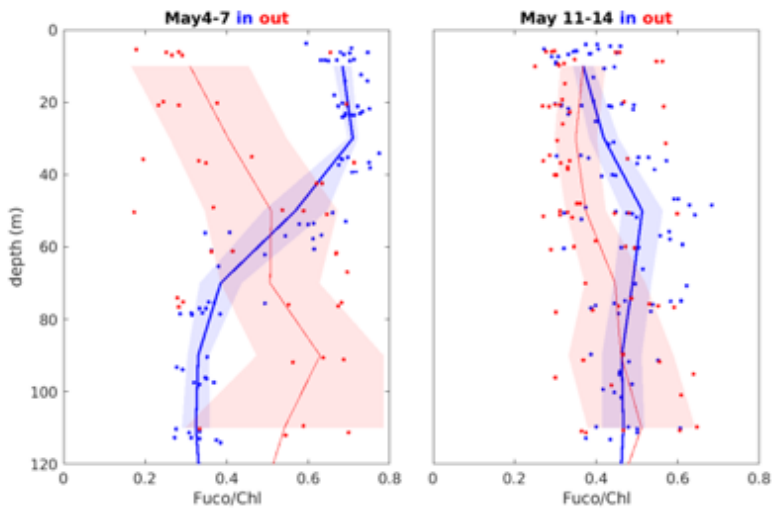
1062 Supplementary Information:

1063



1064

1065 Fig S1 - Satellite Chl and SSH of the eddy field with track of Lagrangian float and wind  
1066 stress time series showing ship work stoppages.



1067

1068 Supplemental Figure 2 - Vertical profiles of ratios of the fucoxanthin (biomarker pigment  
 1069 for diatom abundances) to total chlorophyll a concentrations (Fuco/Chl) and the silicate  
 1070 to nitrate concentrations ( $\text{SiO}_4/\text{NO}_3$ ) in the eddy (blue) and outside the eddy (red) both  
 1071 before (May 4-7) and after (May 11-14) the first large storm. In the eddy is defined as  
 1072 stations located within 15 km of the analyzed eddy center and outside of the eddy is  
 1073 defined as those stations that are 15 to 60 km from the eddy center.

1074

1075

1076 Table S1: Integrated POC and Particle Volume Inventories and Fluxes During Trap  
 1077 Deployments

1078

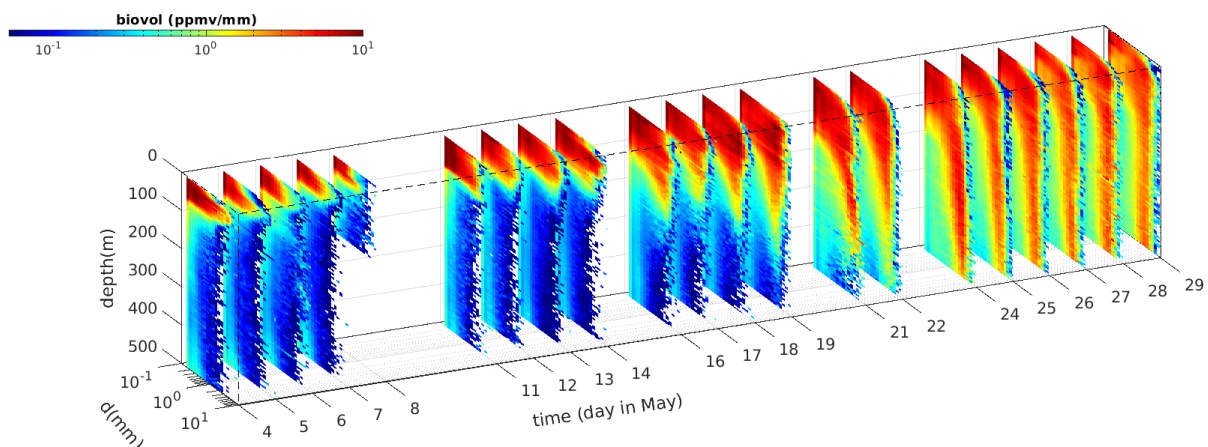
Trap deployment	Units	1	2	3
Dates		May 5-11	May 12-15	May 22-24
Integrated NPP	mmolC m <sup>-2</sup> d <sup>-1</sup>	119	120	53
Integrated POC	mmolC m <sup>-2</sup>	829	812	788
POC Turnover Time by NPP	day	7.0	6.7	14.9
Trap Type & Depth		75 m STT	75 m STT	105 m NBST
POC export	mmolC m <sup>-2</sup> d <sup>-1</sup>	11	9	22
e-ratio	-	0.09	0.08	0.41
POC Turnover Time by Export	day	75	90	36
Integrated Particle Volume	ml m <sup>-2</sup>	421	1366	1279
Particle Volume Flux @ 100 m	ml m <sup>-2</sup> d <sup>-1</sup>	69	435	1273
Particle Volume Turnover Time	day	8.2	3.3	1.1

1079

1080 Notes: Determinations of water column integrated NPP rates from Table 1 in Meyer et al. (2023)  
 1081 are averaged over the periods of the three trap deployment periods. Integrated POC stocks  
 1082 were calculated from available POC profiles water samplings profiles and averaged over the  
 1083 periods of the three trap deployments. Integrated POC export fluxes are determined using the  
 1084 shallowest depths available (Fig. 4b). E-ratios are calculated as the POC export flux at the base  
 1085 of the euphotic zone normalized by the NPP rate. Upper 100 m particle volume inventories and  
 1086 fluxes are calculated as in Figure 3d. Turnover times are calculated as the integrated POC or  
 1087 particle volume inventory in the upper 100 m divided by the export flux or for POC divided by  
 1088 NPP. STT is surface tethered trap array and NBST is Neutrally Buoyant Sediment Trap.

1089

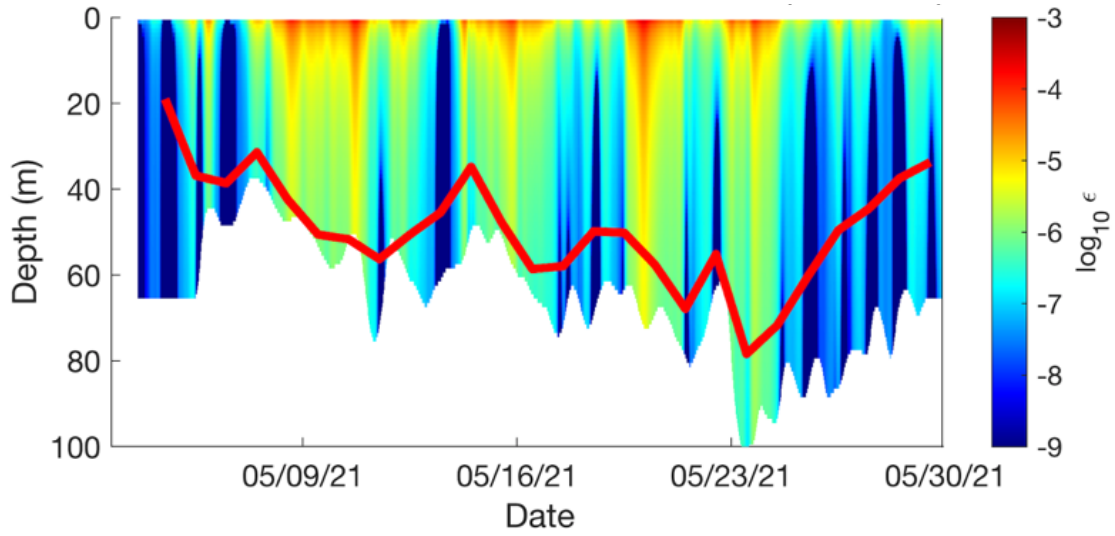
1090



1091

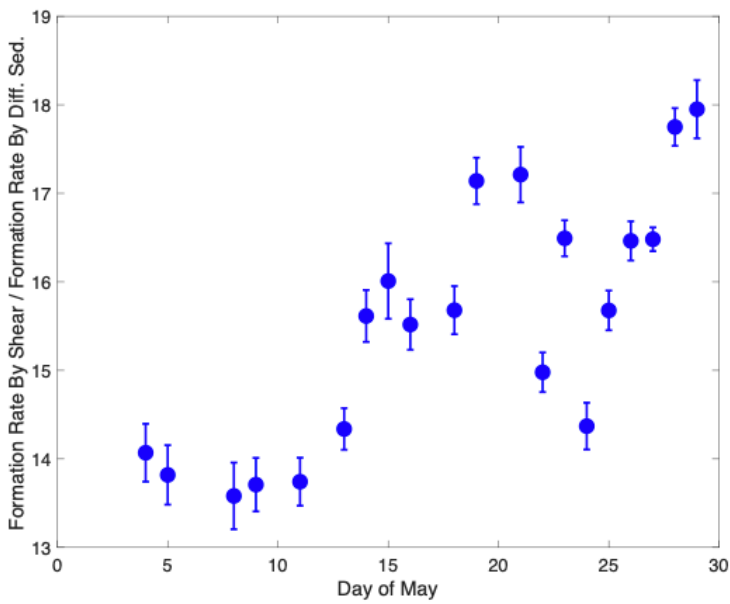
1092 Figure S3: Daily mean profiles of the particle volume spectra (ppmV/mm) for all days during  
 1093 EXPORTS NA both within 15 km to the eddy center.

1094  
1095



1096  
1097  
1098  
1099  
1100

Figure S4: Upper layer contour of KE\_Diss from air-sea flux scaling relationships. Daily mean mixed layer depth is shown in the solid red line.



1101  
1102  
1103  
1104  
1105

Figure S5: The ratio of large (> 5 mm) particle formation rate by turbulent shear to that by differential sedimentation for particles in the 40–80 m depth-range.

1106 Table S2: Normalized Large Particle-Zooplankton Encounter Rates for the Mesopelagic

1107

Depth Interval (m)	Zooplankton Abundances (# m <sup>-2</sup> )		Large (D> 0.51 mm) abundances (# m <sup>-3</sup> )			Normalized Encounter Rates			
	May 17	May 26	May 17	May 17	May 17	May 26	May 11	May 17	May 26
200-300	10236	23243	2.0	2.0	2.0	23243	5.21x10 <sup>3</sup>	1.24x10 <sup>4</sup>	7.88x10 <sup>4</sup>
300-400	20724	23528	0.9	0.9	0.9	23528	3.58x10 <sup>3</sup>	4.30x10 <sup>4</sup>	6.34x10 <sup>4</sup>
400-500	18333	21585	0.6	0.6	0.6	21585	3.54x10 <sup>3</sup>	3.01x10 <sup>4</sup>	4.75x10 <sup>4</sup>

1108 Notes: Large particles are defined as those with D > 0.51 mm and zooplankton abundances are averaged from paired day-night tows  
 1109 (see *Methods*). Encounter rates are available for May 11, 17 and 26, all normalized to the vertical profile on May 11.

1110